Acta Geologica Polonica, Vol. 76 (2026), No. 1, e66
DOI: 10.24425/agp.2026.158180

Petrography, geochemistry, and detrital zircon geochronology of Zongzhuo Formation sandstones in southern Tibet: insights into the tectonic evolution and provenance model of the Tethys Himalaya during the Late Cretaceous

YUHANG FAN[1], FENG DING[1] and XIANGANG XIE[2]

[1] *College of Earth and Planetary Sciences, Chengdu University of Technology, Chengdu 610059, People's Republic of China; e-mails: fanyuhang0726@163.com; 22847785@qq.com*
[2] *State Key Laboratory of Lithospheric and Environmental Coevolution, Institute of Geology and Geophysics, Chinese Academy of Sciences, Beijing 100029, People's Republic of China*

ABSTRACT:

Fan, Y., Ding, F. and Xie, X. 2026. Petrography, geochemistry, and detrital zircon geochronology of Zongzhuo Formation sandstones in southern Tibet: insights into the tectonic evolution and provenance model of the Tethys Himalaya during the Late Cretaceous. *Acta Geologica Polonica*, **76** (1), e66.

Upper Cretaceous Zongzhuo Formation sandstones in the Tethyan Himalaya record critical provenance shifts linked to the India–Asia collision. Petrographic, geochemical, and detrital zircon U-Pb data classify sandstones into three types: Type I (high maturity, quartz/feldspar-rich, passive margin), derived from the Indian craton, with REE patterns mirroring Jurassic passive margin sediments, indicating long-distance transport during ongoing Neo-Tethys subduction; Type II (mixed felsic-mafic composition), reflecting dual sourcing from the Indian craton and the Lhasa Terrane, marking the end of Neo-Tethys subduction and transition to initial collision; and Type III (low maturity, lithic/OIB-type REE, high TiO_2), near-source Lhasa arc volcanics with young zircons (~100–70 Ma), signaling active collision and foreland basin development via India underthrusting. Provenance evolution – from purely Indian (Type I) to mixed (Type II) and dominantly Lhasa-derived (Type III) – constrains the collision onset to ~70–66 Ma. This shift coincides with the Tethyan Himalaya's transformation from a passive margin to a foreland basin, driven by India–Asia convergence. The data challenge Paleogene collision models, emphasizing Late Cretaceous tectono-sedimentary responses as the key markers of collision initiation. These findings provide robust sedimentological evidence for reconstructing collision dynamics and refining regional tectonic timelines.

Key words: Tethys Himalaya; Upper Cretaceous; Zongzhuo Formation; Tectonic evolution; Provenances feed model

INTRODUCTION

The Tethys Himalayan tectonic belt entered a unique geological phase during the Late Cretaceous. Having existed as a passive continental margin in northern India from the Late Triassic to the Early Cretaceous, the region began to transform into a foreland basin in the Late Cretaceous as the Indian continent gradually moved northward, leading to the India–Asia continental collision (Pan *et al.* 1997; Zhu *et al.* 2004, 2009, 2013; Gao 2006). During this period, the Upper Cretaceous Zongzhuo Formation (K_2z) mélange was extensively deposited in the northern Tethys Himalayas. As a special geo-

© 2026 Yuhang Fan, Feng Ding and Xiangang Xie. This is an open access article under the CC BY license (http://creativecommons.org/licenses/by/4.0/), which permits use, distribution, and reproduction in any medium, provided that the article is properly cited.

logical structure at a convergent plate boundary, the Zongzhuo Formation mélange potentially contains critical records of the Neo-Tethys subduction and India–Asia collision. Previous studies on the Late Cretaceous Tethys Himalaya evolution have mainly focused on the paleogeography, sedimentary environments, and basic magmatic rocks, with provenance research on the Zongzhuo Formation mostly addressing the source and chronology of lithic sandstones within the later 'mélange block' or 'matrix' deposits (Sun G.Y. *et al.* 2011; Yi *et al.* 2016; Cheng *et al.* 2017; Zhang *et al.* 2017; Fu *et al.* 2018; Huang Y. *et al.* 2018; Zhou *et al.* 2018). However, research on the source rocks and provenances of highly mature sandstones deposited in the early to mid-sedimentary stages of the Zongzhuo Formation is limited. As part of a regional geological survey project with the China Geological Survey, specifically the 1:50,000 regional geological mapping of Tibet's Rongbu area, various types of Zongzhuo Formation sandstones were systematically sampled. The primary research objective was to further examine the tectonic evolution and provenance model of the Tethys Himalayas during the Late Cretaceous by analyzing sandstone petrography, detrital composition, petrogeochemistry, and detrital zircon chronology. This study holds significant scientific value for refining the possible timeframe of the India–Asia continental collision.

GEOLOGICAL SETTING

The study area is situated in the eastern Tethys Himalaya, bordered to the north by the Yarlung-Zangbo Suture Zone (YZSZ) from the Lhasa block and to the south by the South Tibet Detachment System (STDS) from the Higher Himalaya belt (HHB) (Wang C.S. *et al.* 2000; Nie *et al.* 2005; Huang X.D. 2011; Xu Z.Q. 2011). From the Late Triassic to the Early Cretaceous, the area was located within the passive continental margin of the northern Paleo-Indian continent. Following extensive marine sedimentation, the Early to Late Cretaceous saw the northward movement of the Indian continental segment of the Gondwana paleocontinent, culminating in its collision with the Asian continent and incorporation into the Tethys Himalayas (DeCelles *et al.* 2000, 2004; Gao 2006; Ali and Aitchison 2008; Sun G.Y. *et al.* 2011; Hu *et al.* 2015; Chen X. *et al.* 2016). Therefore, the study area transitioned from a passive continental margin (Late Triassic–Early Cretaceous) to a foreland basin during the Late Cretaceous and eventually participated in Cenozoic continental collision orogeny. This region provides one of the most comprehensive records for studying the Gondwana breakup, Neo-Tethys subduction, and Tibetan Plateau formation.

The Rongbu area falls within the Kangma-Longzi stratigraphic region of the Himalayan stratigraphy, characterized by a NW-SE trending unit that spans tens of kilometers (Xia *et al.* 1997; Xu K.Z. *et al.* 2019). The area is characterized by intense tectonic and magmatic activities, with NW-SE trending faults and folds influencing the strata. Mesozoic strata are well-exposed, primarily of Jurassic and Cretaceous age, and ordered from oldest to youngest as follows: Lower–Middle Jurassic Lure Formation ($J_{1\text{-}2}l$), Middle Jurassic Zhela Formation (J_2z), Upper Jurassic Weimei Formation (J_3w), Upper Jurassic–Lower Cretaceous Sangxiu Formation (J_3-K_1s), Lower Cretaceous Jiabula Formation (K_1j) and Upper Cretaceous Zongzhuo Formation (K_2z^1-K_2z^2) (Text-fig. 1). The Zongzhuo Formation is thicker and sits with a parallel unconformity above the Jiabula Formation, exhibiting a complex lithology (Table 1). The measured stratum histogram is shown in Text-fig. 2. The lower member (K_2z^1) primarily consists of gray-black paper shale, silty and siliceous shale, mudstone, calcareous mudstone, interbedded quartz sandstones, lithic quartz sandstone, feldspathic quartz sandstone, and occasional basalt or tuff. The upper segment includes thick limestone and marl. The Upper Zongzhuo Formation (K_2z^2) continues as an argillaceous deposit with increased limestone and sandstone layers. Unlike the lower member, it primarily features lithic sandstone and graywacke, with the 'matrix' containing numerous exotic sandstones and limestone blocks.

PETROGRAPHY

The sandstones within the 'matrix of the Zongzhuo Formation are generally of three types. Type I lithic quartz sandstones, deposited early in the lower member of the Zongzhuo Formation (e.g., B01 and B02; Text-fig. 3) primarily consist of rounded, monocrystalline allotriomorphic quartz (~83%) with grain sizes ranging from 0.25 to 0.50 mm, accompanied by minor feldspar (<5%) and lithic grains (~10%). The lithic grains mainly consist of sedimentary and volcanic debris, and the feldspar is predominantly plagioclase with polysynthetic twinning. Type I sandstones demonstrate a high maturity of their components and structure, are grain-supported, and are cemented by minor cementing materials, indi-

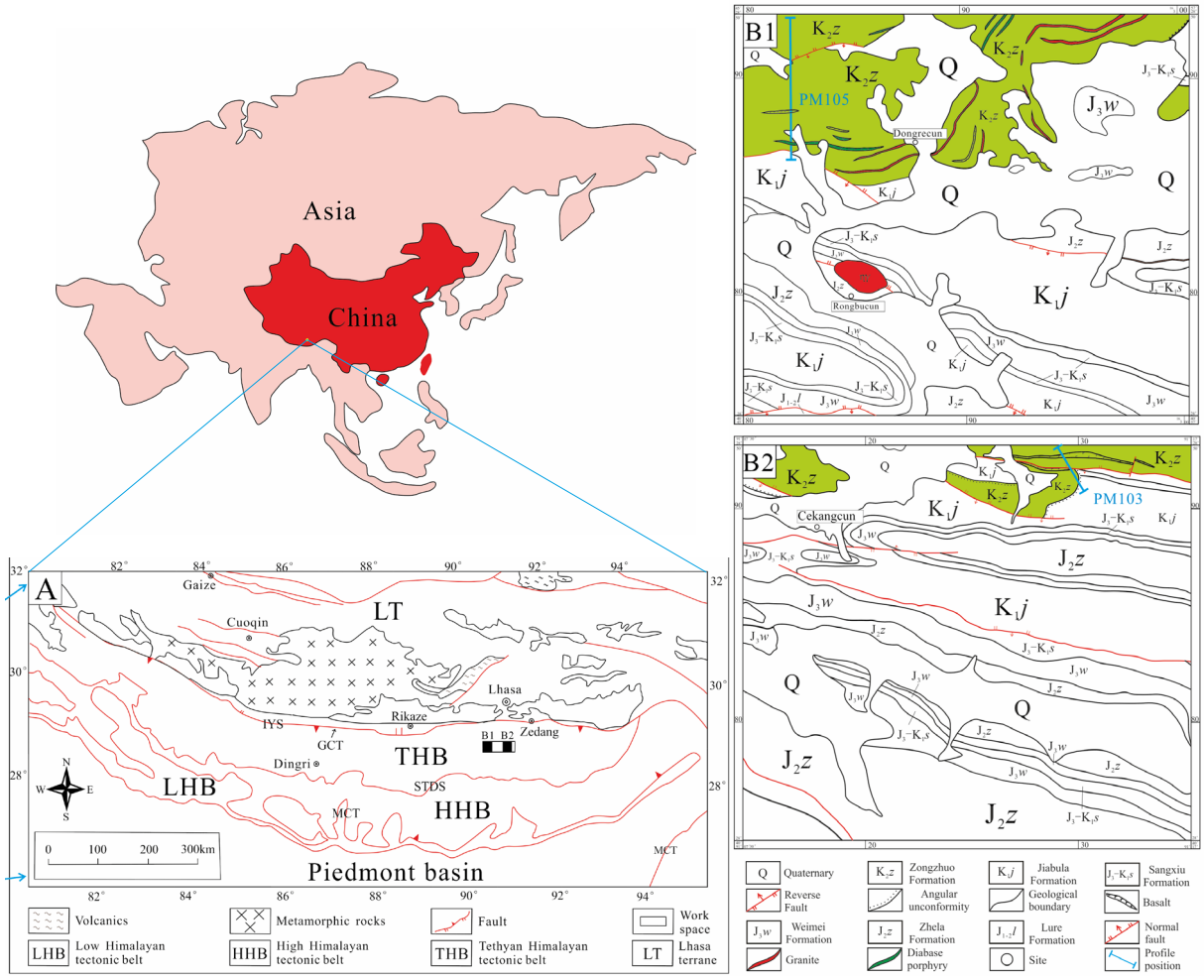

Text-fig. 1. Broader geological tectonic map of southern Tibet (A) (after Nie *et al.* 2005) and detailed geological maps of the study area (B1 and B2).

cating that their sedimentary components underwent extensive transport prior to deposition.

Type II lithic quartz sandstones from the upper member of the Zongzhuo Formation (B03–B06; Text-fig. 3) predominantly consist of rounded monocrystalline allotriomorphic quartz (~77%) and exhibit slightly lower maturity than Type I sandstones. While their mineralogy is similar to that of Type I, the grains are notably smaller (0.10–0.30 mm), primarily fine sands. The feldspar content is largely consistent with that of Type I, but Type II sandstones present a noticeable increase in debris content (~18%) and are predominantly composed of carbonate and volcanic debris.

Type III lithic sandstone or lithic graywacke samples from the upper member of the Zongzhuo Formation (B07 and B08; Text-fig. 3) exhibit near-source deposition, with sandstone fragments primarily composed of debris grains and substantial feldspar. The debris fragments are mainly volcanic, consisting of microcrystalline plagioclase aggregates or pyroxene, likely derived from weathered basic volcanic rocks. Type III sandstones contain minimal metamorphic and sedimentary debris, a relatively low quartz content (>10%), and demonstrate notably low levels of their components and structural maturity. The outcrop characteristics are shown in Text-fig. 4.

SAMPLING AND ANALYTICAL METHODS

All the sandstone samples in this study were collected from various beds in the Upper Cretaceous Zongzhuo Formation (K_2z) in the Rongbu area. Eight samples free from significant weathering, tectonic

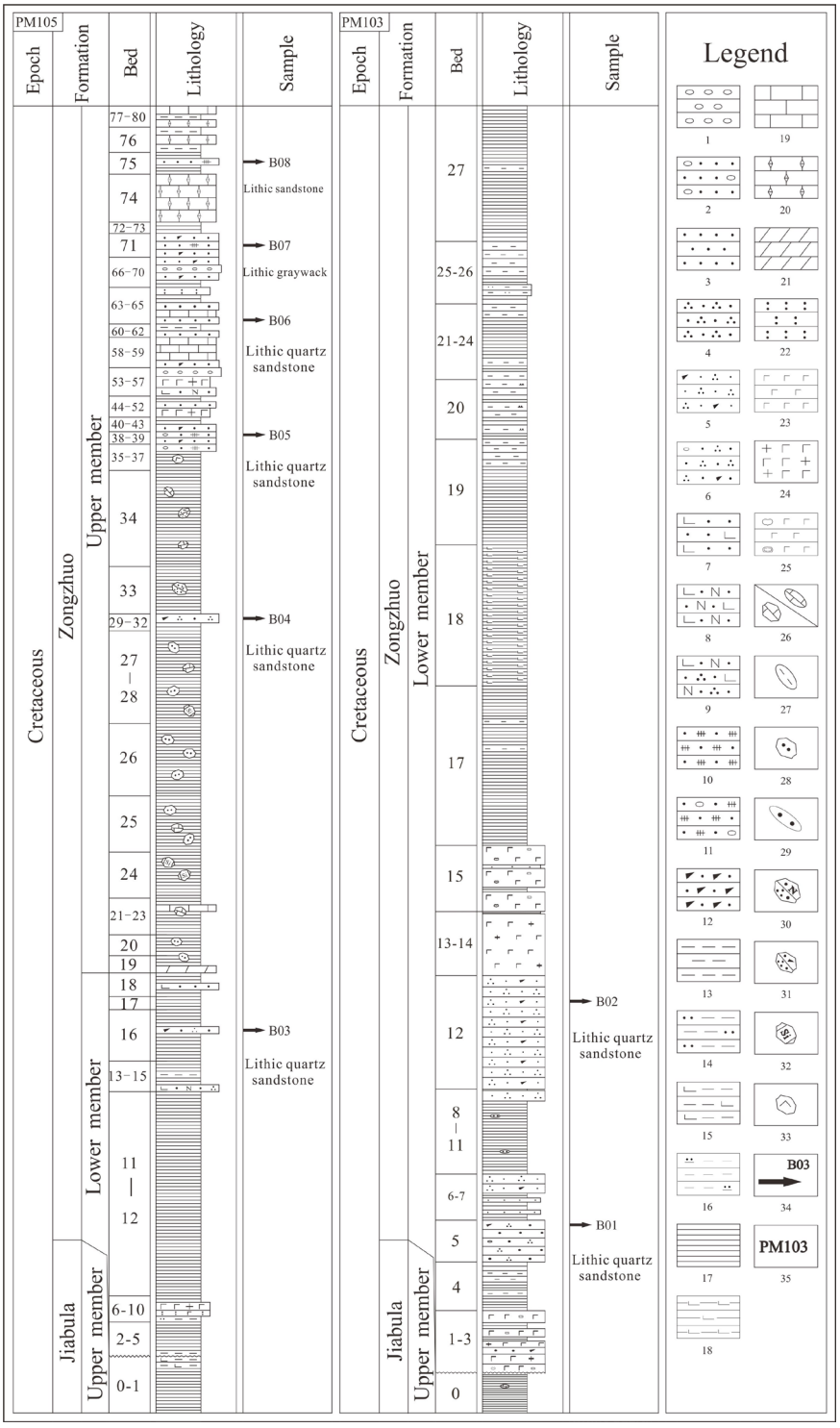

Text-fig. 2. Measured stratigraphic column of the Upper Cretaceous Zongzhuo Formation (K_2z) in the Rongbu area, southern Tibet, China. Explanations: 1 – conglomerate; 2 – pebbly sandstone; 3 – sandstone; 4 – quartz sandstone; 5 – lithic quartz sandstone; 6 – shingly quartz arenite; 7 – arkose; 8 – calcareous feldspathic arenite; 9 – calcareous feldspathic quartz arenite; 10 – graywacke; 11 – pebbly graywacke; 12 – lithic sandstone; 13 – mudstone; 14 – silty mudstone; 15 – calcareous mudstone; 16 – siliceous mudstone; 17 – shale; 18 – calcareous shale; 19 – limestone; 20 – micrite; 21 – marl; 22 – tuff; 23 – basalt; 24 – porphyritic basalt; 25 – amygdaloidal basalt; 26 – limestone blocks; 27 – mudstone lens; 28 – sandstone blocks; 29 – sandstone lens; 30 – feldspathic quartz sandstone blocks; 31 – lithic quartz sandstone blocks; 32 – siliceous blocks; 33 – basalt blocks; 34 – sample location; 35 – profile number.

PM105			
Formation	**Bed**	**Thickness [m]**	**Main rock types**
Zongzhuo	77–80	75.93	micrite, mudstone
	76	88.19	mudstone, micrite
	75	78.51	shale, with interlayers of sandstone
	74	170.12	micrite, calcareous mudstone
	72–73	79.4	celadon shale
	71	123.61	lithic sandstone
	66–70	107.6	lithic sandstone-conglomerate-lithic sandstone-conglomerate composed of rhythmic beds cyclothems
	63–65	130.35	Upper: tuff; Lower: sandstone, limestone bands
	60–62	46.52	mudstone, sandstone bands
	58–59	108.14	thick-massive microcrystalline limestone
	53–57	99.67	Upper: conglomerate; Middle: porphyritic basalt; Lower: feldspathic quartz sandstone
	44–52	75.95	Upper: shale; Middle: gritstone; Lower: porphyritic basalt
	40–43	51.84	lithic sandstone
	38–39	42.71	greywacke
	35–37	93.82	shale and basalt block
	34	339.7	shale, lithic quartz sandstone, limestone rocks
	33	45.57	shale, feldspathic quartz sandstone blocks
	29–32	86.6	shale, quartz sandstone
	27–28	328.3	shale, siliceous rocks, sandstone rocks
	26	256.8	shale, sandstone rocks
	25	198.1	shale, siliceous rocks
	24	163.9	shale, limestone
	21–23	128.8	shale, limestone band and rocks
	20	72.9	shale, exotic block
	19	62.8	shale, marl
	Lower member (K_2z^1) >1358.6 (m) Conformable contact		
	18	84.3	shale, calcareous sandstone
	17	46.5	shale
	16	182.9	shale, sandstone band
	13–15	107.6	Lower: calcareous feldspathic quartz arenite; Upper: shale, mudstone
	11–12	723.6	shale
	6–10	92.1	volcanic rock, porphyritic basalt, basaltic tuff
	2–5	121.6	Upper: shale; Lower: celadon mudstone
Jiabula	0–1	58.2	Lower: shale, silty mudstone; Upper: calcareous mudstone
PM103			
Formation	**Bed**	**Thickness [m]**	**Main rock types**
Zongzhuo	27	189.6	shale, mudstone
	25–26	42.4	mudstone, shale
	21–24	53.6	mudstone, shale
	20	45.7	silica mudstone
	19	73.5	shale, mudstone
	18	99.1	calcareous shale
	16–17	115.4	shale, mudstone
	15	46.5	amygdaloidal basalt, shale, sandstone
	13–14	45.4	porphyritic basalt, microlitic basalt
	12	156.8	lithic quartz sandstone
	8–11	59	shale and lenses of sandstone
	6–7	32.7	shale, sandstones
	5	31.8	lithic quartz sandstone
	4	38.3	shale, mudstone
	1–3	42.0	amygdaloidal basalt, pillow basalt
Jiabula	0	37.2	marl, shale

Table 1. Lithological description of the Zongzhuo Formation (PM103, PM105).

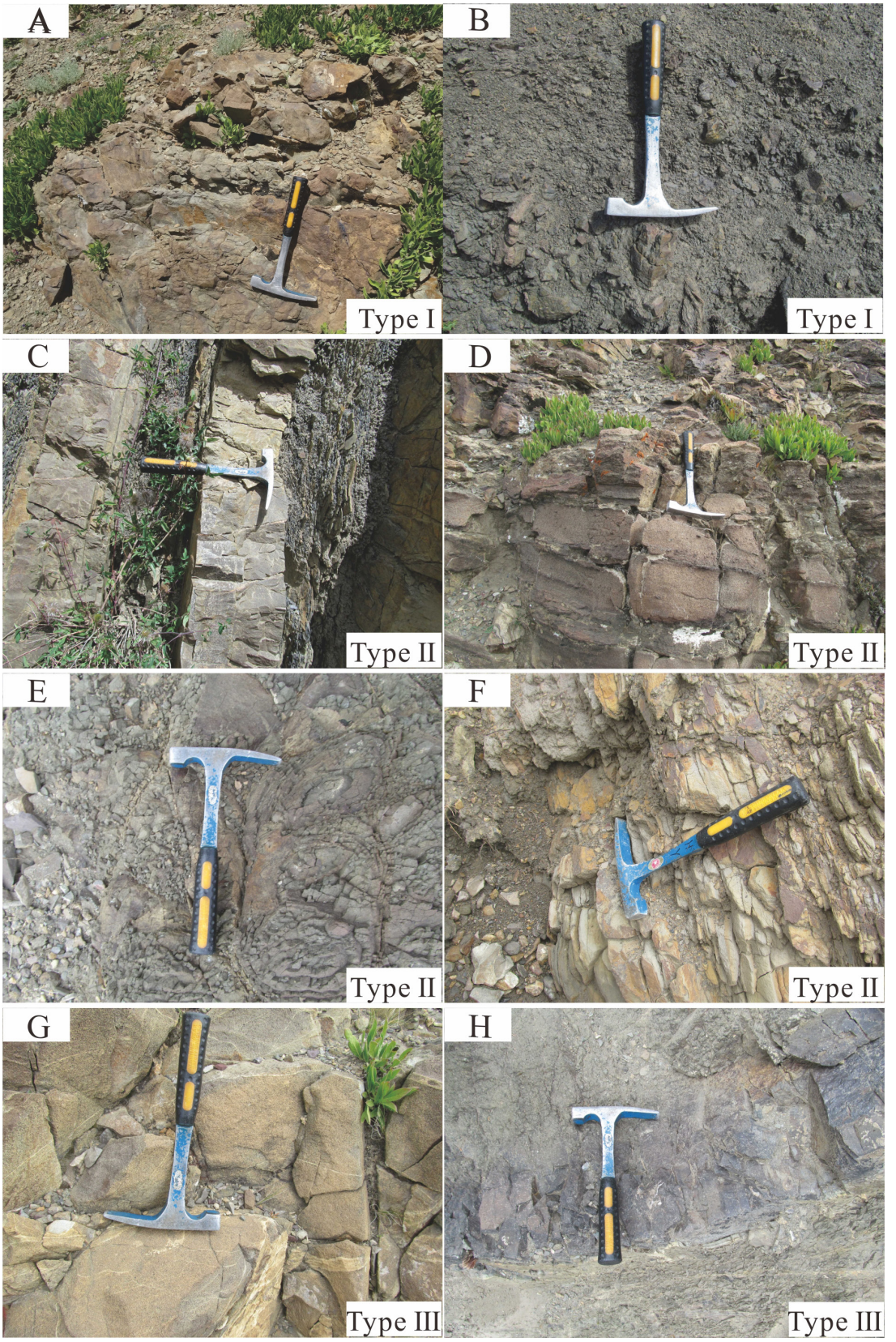

Text-fig. 3. Field photographs of Zongzhuo Formation sandstones in Langka County, Tibet, China.

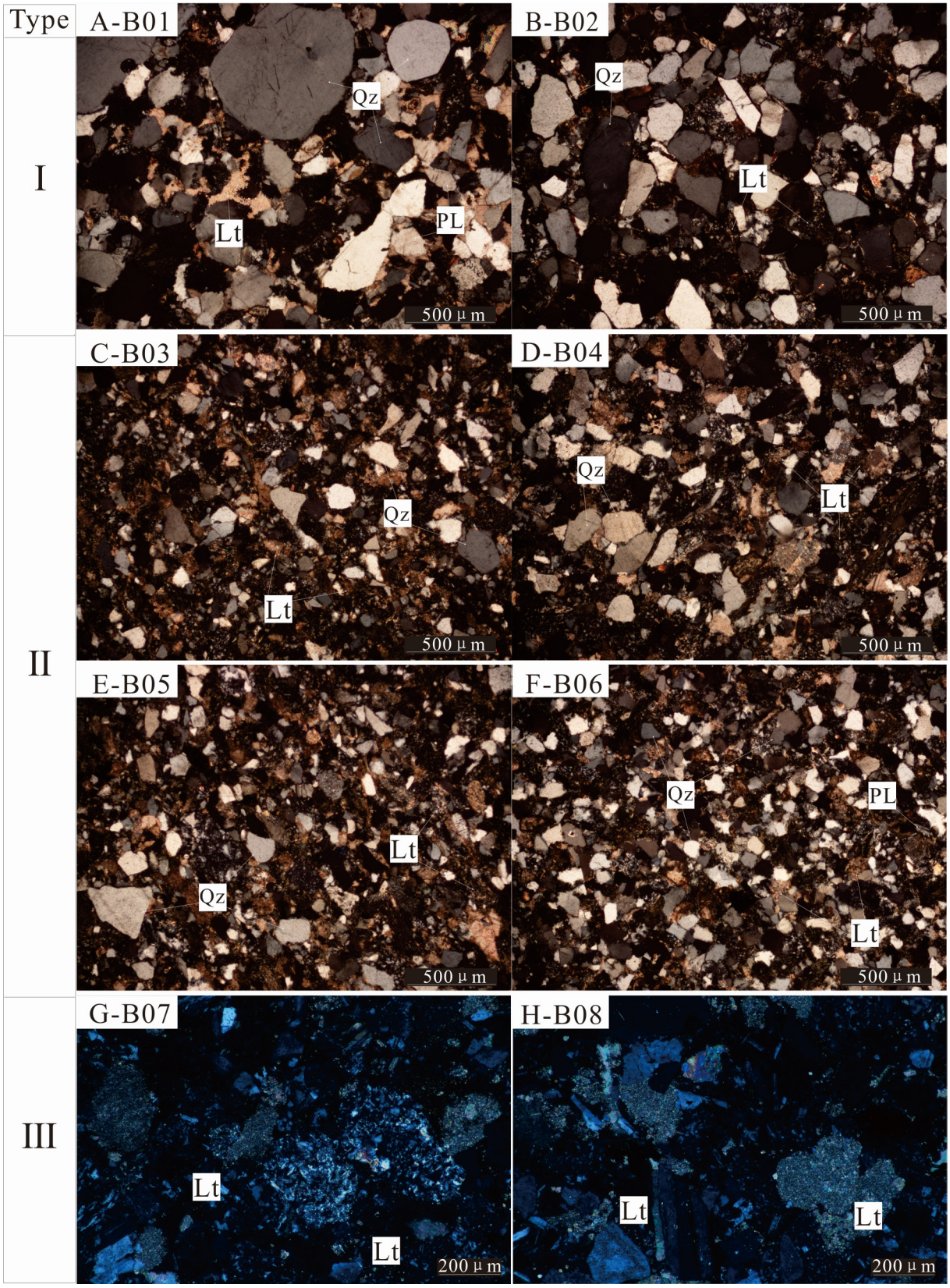

Text-fig. 4. Microphotographs of Zongzhuo Formation sandstones. Explanations: Qz – quartz; PL – feldspar; Lt – lithic clast.

fractures, alteration, and metamorphism were selected for analysis, and their respective sampling beds are illustrated in Text-fig. 2. To capture the varied provenance characteristics of the Zongzhuo Formation sandstones across different sedimentary intervals, samples were systematically extracted from the measured stratigraphic profiles. Type I (B01 and B02), Type II (B03–B06), and Type III (B07 and B08) sandstones were collected from the lower, middle, and upper sections of the Zongzhuo Formation, respectively, representing the early, middle, and late clastic deposits. Thin section analyses, fragment composition statistics, whole-rock geochemistry, and detrital zircon U-Pb dating (for lithic sandstone sample B07) were completed for all samples.

Microscopic identification and statistical analysis of clastic components in sandstone samples were conducted at the State Key Laboratory of Oil and Gas Reservoir Geology and Exploitation, Chengdu University of Technology, China. Sandstone samples with matrix content exceeding 25% were excluded. For each sample, over 350 fragments were counted using the Dickinson-Gazzi point method to ensure accuracy (Gazzi 1966; Dickinson 1970).

Whole-rock geochemistry, including major, trace, and rare earth elements (REEs), was analyzed at the Chengdu Southwest Metallurgical Geological Testing Center, China. The major elements were measured on an AxiosX fluorescence instrument using fluorescence, gravimetric and titration methods, achieving an analytical precision below 2% in compliance with GB/T14506.28 2010 and DZG20-02 standards. For ICP-atomic emission spectrometry (ICP-AES), ICP-mass spectrometry (ICP-MS), and amplite fluorescence spectrometry (AFS), the precision was maintained below 1% error. Trace elements were determined via AxiosX fluorimetry, iCAP6300 spectrometry, and NexLON 300x ICP-MS, following X-ray fluorescence methods according to the DZG20-05 and DZG20-06 standards. REEs were analyzed on a NexLON 300x ICP-MS using mass spectrometry according to DZG20-06, with all measurements conducted under controlled conditions of 23ºC and 59% humidity.

Zircon grains were hand-picked, mounted in epoxy resin, and polished by Honesty Geological Services in Langfang, China. Cathodoluminescence (CL) and transreflection micrographs of these zircon grains were prepared by the Navigation Technology Limited Company, Beijing, China. The bulk rock samples were crushed to a grain size of less than 60 mesh. Zircon was first concentrated using the heavy mineral separation method, followed by handpicking under a binocular microscope. Approximately 199 to 224 zircon grains were initially selected from each sample. The selected zircon grains were mounted on double-sided adhesive tape, fixed in transparent epoxy resin, and then polished together with the resin until the interiors of the zircons were exposed, making them suitable for LA-ICP-MS analysis. After polishing, the zircons were examined using reflected light and transmitted light microscopy, as well as cathodoluminescence (CL) imaging. Based on the CL images, a secondary selection was carried out: grains with blurred zoning, broken edges, perforations or fractures were discarded, while those with clear oscillatory zoning, straight edges or intact outlines were retained for analysis. The analytical spots on the selected zircons were carefully positioned using reflected and transmitted light images to avoid surface fractures and internal inclusions, ensuring data quality. following the methods outlined by Song *et al.* (2002). During testing, clear and texturally intact zircon grains free from cracks or inclusions were selected, with CL images revealing the internal structures and oscillatory zones to identify appropriate dating locations.

U–Pb dating of detrital zircons was performed using LA-ICP-MS at the State Key Laboratory of Geological Processes and Mineral Resources (GPMR), China University of Geosciences, Wuhan, China. Laser ablation was conducted using a GeoLas2005 with an Agilent 7500a ICP-MS employing a 30 μm diameter laser beam. The international standard zircon 91500 (1064 Ma) from Harvard University was used as the external standard for isotope fractionation correction. For every five sample points, the 91500 standard was analyzed twice (Wiedenbeck *et al.* 1995; Liu *et al.* 2010). Data processing was completed using ICP MS Data Cal, while age calculations and concordia diagrams were generated using Isoplot 4.0 (Liu *et al.* 2008; Chen L. *et al.* 2011; Ludwig 2011).

RESULTS

Detrital compositions

The statistical results for detrital fragments in the Zongzhuo Formation sandstones are summarized in Table 2. In Type I lithic quartz sandstones, the total quartz grains (Qt) and monocrystalline quartz grains (Qm) constituted high percentages of 83.33–86.01% and 79.27–81.54%, respectively. The total unstable lithic fragments (L) and polycrystalline lithic frag-

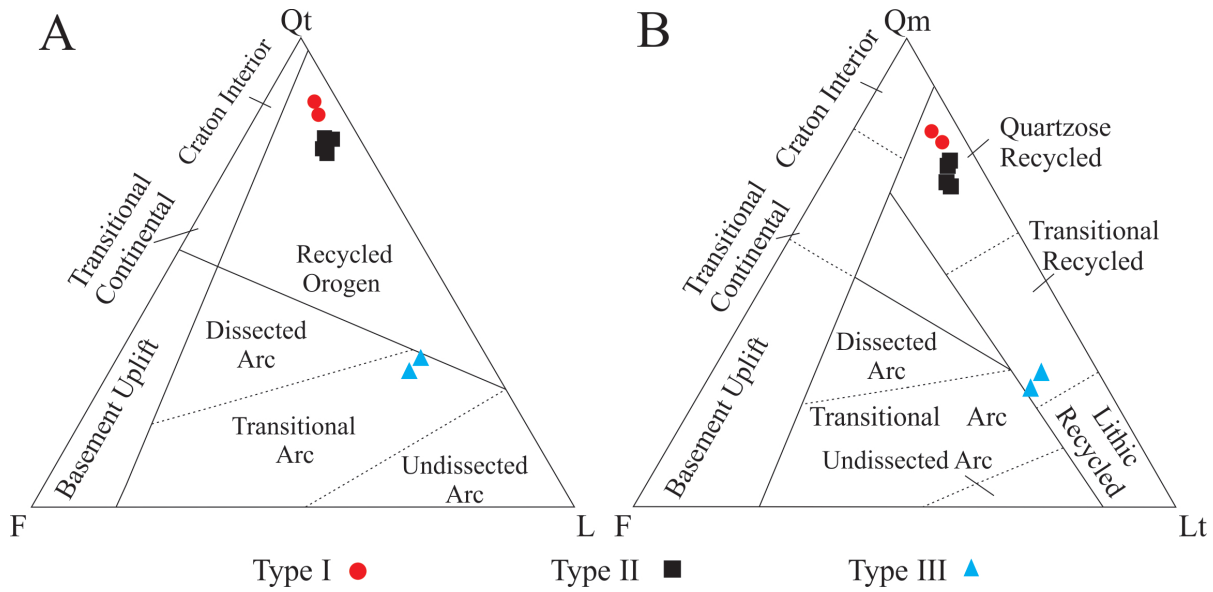

Text-fig. 5. Petrography of the Weimei Formation sandstones plotted on standard (A) Qt–F–L and (B) Qm–F–Lt diagrams (after Dickinson *et al.* 1983).

ments (Lt) accounted for 9.33–11.28% and 13.07–16.06%, respectively. In Type II sandstones, the Qt and Qm percentages decreased to 75.28–78.10% and 69.66–75.18%, respectively, while the L and Lt contents increased to 14.68–16.85% and 19.46–22.47%, respectively. Type III sandstones were primarily composed of lithic fragments, with significantly lower Qt and Qm percentages of 28.71–31.57% and 26.08–29.74%, respectively, while the L and Lt percentages increased to 55.35–56.14% and 58.02–58.24%, respectively. These fragment statistics are aligned with the petrological characteristics of the sandstones.

The provenance discrimination diagrams (Text-fig. 5) illustrate that Type I sandstones were plotted within the recycled orogen fields close to the craton interior field, suggesting that their sedimentary materials were primarily derived from recycled sedimentary or metamorphic rocks. Type II lithic quartz sandstones demonstrated a plot similar to that of Type I, with slightly lower quartz and markedly higher debris content, positioning them near the center of the recycled orogen field. In contrast, Type III sandstones or graywackes were plotted within the transitional arc or transitional recycled fields, reflecting their low quartz content and substantial increase in debris and feldspar, which was indicative of a provenance near island-arc volcanic rocks (Dickinson and Suczk 1979; Dickinson *et al.* 1983; Dickinson 1985).

Sandstone type	Sample	Lithology	Qt	F	L	Qm	F	Lt	Total
Type I	B01	lithic quartz sandstone	325	21	44	318	21	51	390
	B02	lithic quartz sandstone	332	18	36	306	18	62	386
Type II	B03	lithic quartz sandstone	326	35	68	303	35	91	429
	B04	lithic quartz sandstone	361	30	69	348	30	92	470
	B05	lithic quartz sandstone	321	22	68	309	22	80	411
	B06	lithic quartz sandstone	335	35	75	310	35	100	445
Type III	B07	lithic greywacke	180	70	320	168	70	332	570
	B08	lithic sandstone	172	95	331	156	95	347	598

Table 2. Detrital composition of the three types sandstones from the Zongzhuo Formation. Explanations: Qt – total quartz grains; F – total feldspar grains; L – total unstable lithic fragments; Qm – monocrystalline quartz grains; Lt – total polycrystalline lithic fragments.

Sandstone Type	Sample	SiO_2	Al_2O_3	Fe_2O_3	FeO	MgO	CaO	Na_2O	K_2O	TiO_2	MnO	P_2O_5	SO_2	LOI	CIA	ICV
Type I	B01	85.3	5.6	1.6	1.6	0.46	0.72	1.43	0.25	0.64	0.07	0.10	1.720	1.86	72.92	1.15
	B02	85.0	7.5	1.8	0.6	0.21	0.31	0.08	1.14	0.42	0.02	0.12	2.500	2.78	86.65	0.55
Type II	B03	71.3	10.7	0.8	3.5	1.55	2.51	2.30	1.07	0.50	0.06	0.12	2.710	4.94	66.09	1.12
	B04	72.5	6.8	1.3	3.3	1.03	5.81	1.00	0.78	0.42	0.08	0.09	2.020	6.44	70.93	1.31
	B05	66.9	8.7	0.9	3.6	2.48	6.17	1.66	0.84	0.49	0.08	0.12	0.023	7.59	67.61	1.35
	B06	78.0	8.4	0.1	4.6	1.94	0.76	1.69	0.72	0.44	0.04	0.10	0.021	2.62	74.72	1.18
Type III	B07	45.6	14.3	5.8	5.6	5.01	6.06	6.62	0.74	2.82	0.16	0.39	5.380	6.39	54.09	2.20
	B08	45.1	13.6	4.8	5.9	5.58	7.73	5.98	0.38	2.79	0.18	0.38	4.650	6.92	52.49	2.32

Table 3. Major element concentrations (wt %) and main parameters for sandstone samples of the Zongzhuo Formation. Note: CIA=100*Al_2O_3/(Al_2O_3+CaO*+Na_2O+K_2O); ICV = (Fe_2O_3 + FeO + MgO+ CaO*+ Na_2O + K_2O + TiO_2 + MnO)/Al_2O_3. CaO* represents the CaO content except carbonate minerals and apatites in the sandstones.

Lithogeochemistry

Major elements

The major element characteristics of the Zongzhuo Formation sandstones were divided into three types (Table 3). Type I sandstones exhibited a high SiO_2 content (85.04–85.31%) with low Al_2O_3 and mafic (TFe_2O_3 + MgO) contents (5.55–7.45% and 2.61–3.78%, respectively). Na_2O, K_2O, and CaO were also low, with CNK (Cao+Na_2O+K_2O) content ranging from 1.53% to 2.40% and TiO_2 from 0.42% to 0.62%. These sandstones were felsic, with minimal feldspar. The CIA and ICV values ranged from 72.91 to 86.64 and 0.55 to 1.15, respectively, indicating the low clay content, extensive sediment transport, and high weathering levels (Nesbitt and Young 1982, 1989; McLennan *et al.* 1993; Cullers 2000, 2002; Feng *et al.* 2003).

Compared with Type I, Type II sandstones had slightly lower SiO_2 contents (66.90–77.98%) and higher Al_2O_3, mafic, and CNK contents (6.80–10.68%, 6.01–7.42% and 3.17–8.66%, respectively), while TiO_2 remained at similar levels (0.42–0.50%). These sandstones contained feldspar and mafic minerals. With lower CIA values (66.09–74.72) and higher ICV values (1.12–1.35), Type II sandstones exhibited a greater clay content, higher weathering levels, and lower maturity than Type I sandstones.

Type III sandstones exhibited notably lower SiO_2 contents (45.05–45.58%) and higher Al_2O_3, mafic and CNK contents (13.63–14.30%, 16.92–17.01% and 13.43–14.09%, respectively), indicating low quartz and high mafic mineral, feldspar and clay contents. The CIA and ICV values for Type III sandstones ranged from 52.49 to 54.09 and 2.20 to 2.32, respectively, indicating short-distance sediment transport, low maturity, and minimal weathering.

Trace elements

The three sandstone types demonstrated distinct differences in trace and rare-earth elements (Text-fig. 6 and Table 4). Type I sandstones exhibited REE

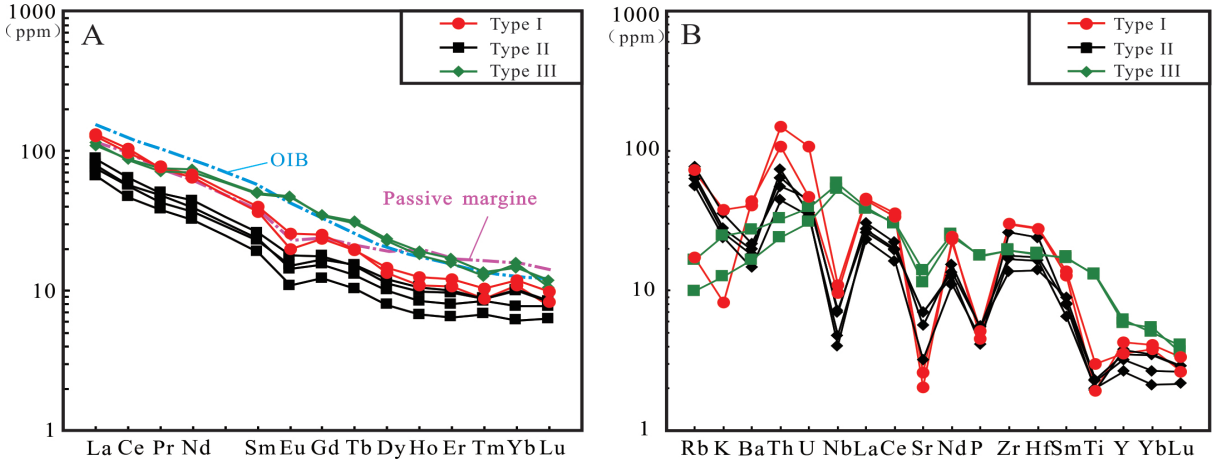

Text-fig. 6. Normalized diagrams for dacite of the Sangxiu Formation, including: A – primitivee mantle-normalized spider diagram; and B – chondrite-normalized REE patterns (values from Sun and McDonough 1989).

Type	Type I			Type II					Type III		
Sample	B01	B02	AVG	B03	B04	B05	B06	AVG	B07	B08	AVG
Ba	303.51	284.88	294.20	150.68	126.06	137.7	102.2	129.16	188.37	115.43	151.90
Cd	0.09	0.04	0.07	0.07	0.07	0.05	0.06	0.06	0.08	0.08	0.08
Co	10.67	6.74	8.71	14.31	11.51	15.14	14.43	13.85	42.03	44.84	43.44
Cr	56.41	38.62	47.52	69.59	111.00	295.34	281.10	189.26	99.43	204.73	152.08
Cs	0.39	1.54	0.96	2.36	2.22	2.56	2.01	2.29	1.33	3.73	2.53
Cu	8.40	6.41	7.41	20.37	12.64	19.00	15.59	16.90	43.05	44.86	43.96
Ga	10.11	10.61	10.36	11.08	6.87	11.08	10.42	9.86	21.19	17.13	19.16
Hf	8.61	8.53	8.57	4.33	7.40	5.35	5.05	5.53	5.66	5.53	5.60
Nb	6.85	7.76	7.30	4.97	2.87	5.13	3.40	4.09	41.49	37.64	39.56
Ni	16.01	9.03	12.52	24.35	29.03	118.96	85.44	64.45	51.39	94.63	73.01
Pb	12.17	21.61	16.89	11.81	14.40	12.25	12.42	12.72	2.53	2.37	2.45
Rb	11.03	45.20	28.12	48.70	39.80	42.35	35.74	41.65	10.47	6.27	8.37
Sr	43.03	54.90	48.97	118.73	147.49	146.56	67.68	120.12	240.96	294.12	267.54
Ta	0.47	0.71	0.59	0.39	0.24	0.38	0.26	0.32	2.52	2.30	2.41
Th	9.09	12.58	10.84	4.69	6.22	5.43	3.76	5.03	2.76	2.03	2.40
U	0.98	2.23	1.61	0.96	0.75	0.90	0.72	0.83	0.82	0.64	0.73
V	65.58	49.01	57.30	92.52	57.79	77.69	74.14	75.54	251.58	245.89	248.74
Zn	54.55	39.42	46.99	55.14	70.80	55.04	52.01	58.25	114.30	106.70	110.50
Zr	336.16	330.80	333.48	153.41	290.83	200	188	208.08	215.71	217.80	216.76
La	30.37	31.24	30.80	20.84	17.88	18.81	15.81	18.33	26.99	25.97	26.48
Ce	59.92	63.46	61.69	39.28	34.54	35.22	28.77	34.45	52.92	54.10	53.51
Pr	7.26	7.19	7.23	4.77	4.09	4.59	3.64	4.27	6.76	7.10	6.93
Nd	31.69	29.92	30.81	20.60	17.15	18.34	14.99	17.77	32.80	34.31	33.56
Sm	6.09	5.66	5.87	3.98	3.52	3.59	2.89	3.50	7.53	7.67	7.60
Eu	1.49	1.16	1.33	1.04	0.89	0.83	0.63	0.85	2.70	2.74	2.72
Gd	5.23	4.86	5.05	3.63	3.44	3.17	2.52	3.19	7.16	7.07	7.11
Tb	0.75	0.73	0.74	0.56	0.58	0.49	0.39	0.50	1.17	1.15	1.16
Dy	3.41	3.70	3.56	2.88	3.08	2.57	2.03	2.64	5.98	5.76	5.87
Ho	0.62	0.71	0.66	0.56	0.60	0.48	0.38	0.51	1.08	1.02	1.05
Er	1.77	2.00	1.89	1.59	1.65	1.33	1.07	1.41	2.81	2.61	2.71
Tm	0.23	0.27	0.25	0.22	0.22	0.21	0.17	0.21	0.35	0.33	0.34
Yb	1.88	2.02	1.95	1.70	1.72	1.31	1.04	1.45	2.48	2.68	2.58
Lu	0.20	0.25	0.22	0.21	0.21	0.20	0.16	0.20	0.30	0.27	0.28
Y	16.22	19.48	17.85	16.05	17.15	14.53	12.02	14.94	28.01	26.45	27.23
ΣREE	150.90	153.17	152.03	101.88	89.57	91.14	74.49	89.27	151.03	152.77	151.90
LREE	136.82	138.64	137.73	90.51	78.06	81.38	66.73	79.17	129.70	131.89	130.80
HREE	14.08	14.53	14.31	11.37	11.51	9.76	7.76	10.10	21.33	20.88	21.10
LREE/HREE	9.72	9.54	9.63	7.96	6.78	8.34	8.59	7.92	6.08	6.32	6.20
La_N/Yb_N	11.61	11.12	11.36	8.78	7.44	10.28	10.85	9.34	7.81	6.94	7.38
δEu	0.81	0.68	0.74	0.84	0.78	0.75	0.71	0.77	1.12	1.14	1.13
δCe	0.99	1.04	1.01	0.97	0.99	0.93	0.93	0.95	0.96	0.98	0.97

Table 4. Trace and rare earth element concentrations (ppm) and main parameters for sandstone samples of the Zongzhuo Formation.

patterns typical of passive margin (PM) deposits, characterized by right-dipping REE distributions, marked Eu-negative anomalies, LREE enrichment, and significant LREE/HREE fractionation (Text-fig. 6A): ΣREE – average: 152.03 ppm, LREE/HREE – average: 9.63 ppm, (La/Yb)N – average: 11.36 ppm, and δEu – average: 0.74 ppm. The trace elements in Type I sandstones revealed enrichment in high field strength elements (HFSEs) such as Th (average: 10.84 ppm), U (average: 1.61 ppm), Zr (average: 333.48 ppm), and Hf (average: 8.57ppm), with a depletion in Nb (average: 7.30 ppm). The large ion lithophile element (LILE) Rb was variable (average 28.12 ppm), whereas K (average: 5771.17 ppm), Ba (average: 294.20 ppm), and Sr (average: 48.97 ppm) primarily presented depletions (Text-fig. 6B).

Type II sandstones exhibited REE and trace element patterns similar to Type I, with LREE en-

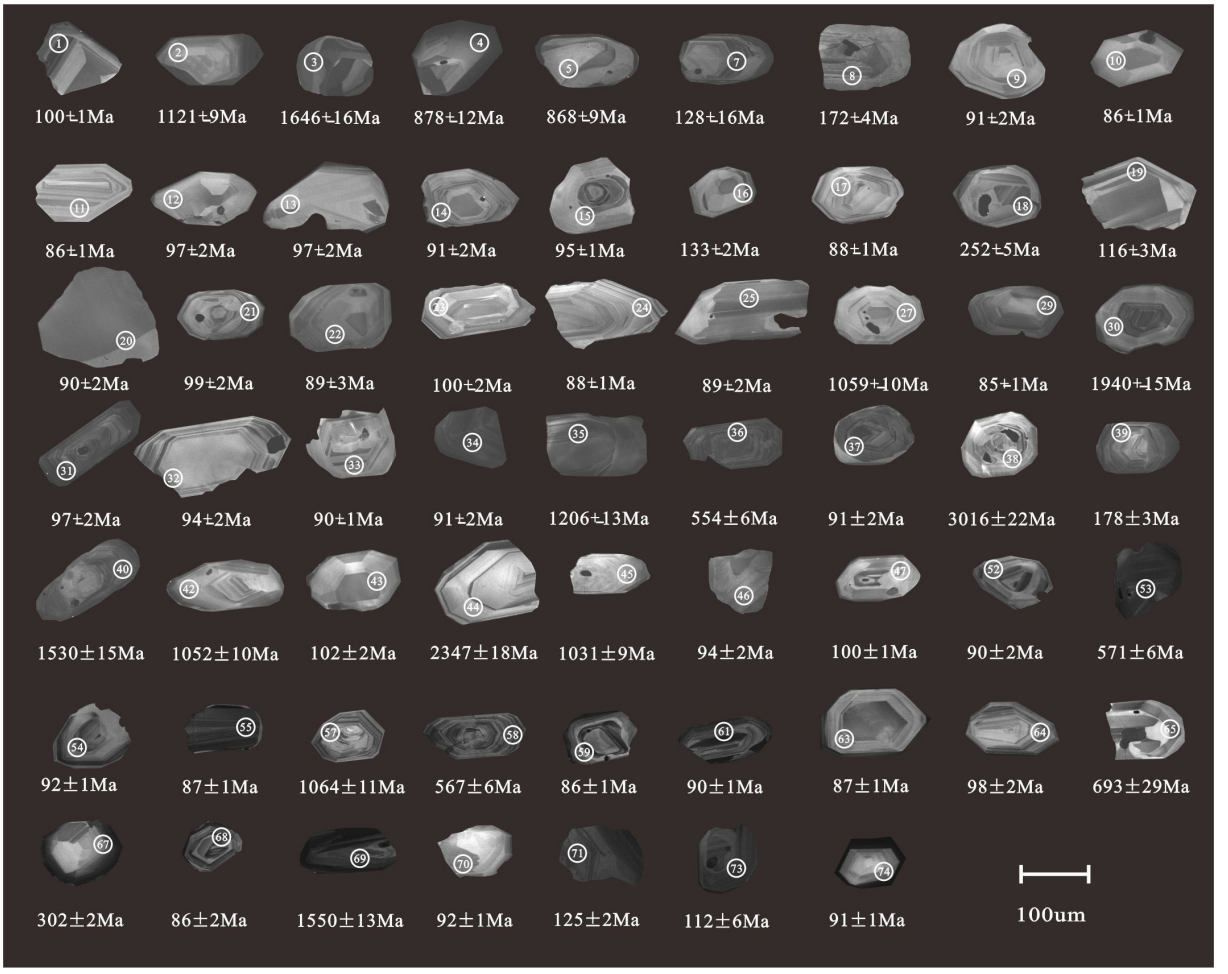

Text-fig. 7. Cathodoluminescence (CL) images of detrital zircons from the Zongzhuo Formation sandstones along with their absolute ages.

richment and high fractionation [averages of LREE/HREE and $(La/Yb)_N$ ratios of 7.92 and 9.34, respectively]. However, Type II sandstones had a slightly lower ΣREE content and a weaker Eu-negative anomaly than Type I, with the averages of 89.27 ppm for ΣREE and 0.77 for δEu. The trace element characteristics aligned with Type I sandstones but generally demonstrated lower element concentrations, with enrichment in Th, U, Zr, Hf, Rb, and depletion in K, Ba, and Sr.

Type III sandstones presented distinct REE and trace element patterns compared with the other two types, with stable right-dipping REE profiles, high ΣREE content, and LREE enrichment (ΣREE averages: 151.90 ppm, LREE/HREE averages: 6.20 ppm, and $(La/Yb)_N$ averages: 7.38 ppm). They exhibited weak Eu-positive anomalies (1.12–1.14) and REE patterns akin to those of the OIB-type volcanic rocks. Their trace element characteristics also differed markedly, with a notable Nb enrichment, typical Th, U, Zr, and Hf levels, and widespread depletions in LILEs, such as Rb, K, Ba and Sr.

Detrital zircon geochronology

A CL image of the zircon grains from sample B07 is shown in Text-fig. 7. Most zircon grains were irregular, with a few idiomorphic grains, and their major and minor axes ranged from 70 to 200 μm and 50 to 150 μm, respectively. The length-to-width ratio varied between 2:1 and 1.2:1. These zircons exhibited clear zonal textures and occasional circular corrosion borders. The Th and U contents ranged from 91 to 3280 ppm and 166 to 2519 ppm, respectively, with most Th/U ratios close to 1. The strong positive correlation between Th and U indicated that the majority of these zircons were of magmatic origin (Hanchar

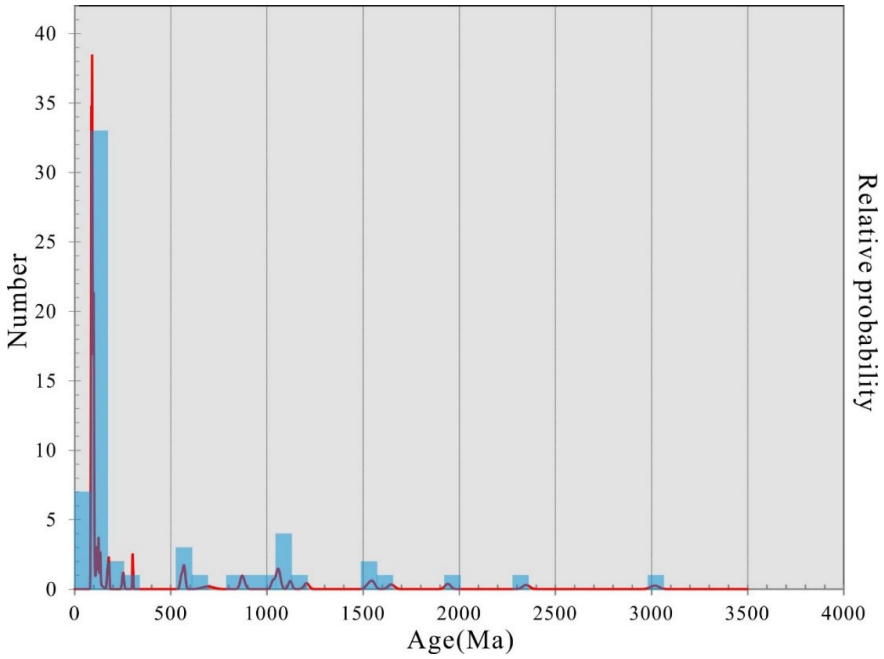

Text-fig. 8. Age distribution map for 74 samples from the Zongzhuo Formation sandstones.

and Miller 1993; Hoskin and Black 2000; Möller *et al.* 2003).

The LA-ICP-MS U-Pb dating of zircons revealed that the detrital zircon ages in the Type III sandstones were primarily concentrated around 90, 500, and 1000 Ma, with a dominant peak at 90 Ma, reflecting the age of most analyzed zircons. The concordance of the individual zircon ages exceeded 90% (Text-fig. 8), confirming the accuracy and reliability of the zircon ages in this study.

DISCUSSION

Weathering

The Zongzhuo Formation in the study area, positioned on the northern margin of the Indian continent, was deposited during the Late Cretaceous. Geophysical research indicates that the Indian continent began its rapid northward movement at the onset of the Late Cretaceous (Yang *et al.* 2015). This shift in paleolatitude likely altered weathering intensity in the source area. As illustrated in the A–CN–K diagram (Text-fig. 9), Type I sandstones deposited during the early stage of the Zongzhuo Formation exhibited high CIA values (72.91–86.64), indicating a hot, humid climate and intense weathering at low latitudes. This suggests that the Indian continent moved near the equatorial tropics during the deposition of Type I sandstones. Type II sandstones with a weathering trend similar to that of andesite demonstrated medium CIA values (66.08–74.72), indicating a transition to middle latitudes with a warm, moist climate and moderate weathering. Type III sandstones deposited in the late stage of the Zongzhuo Formation exhibited significantly lower CIA values

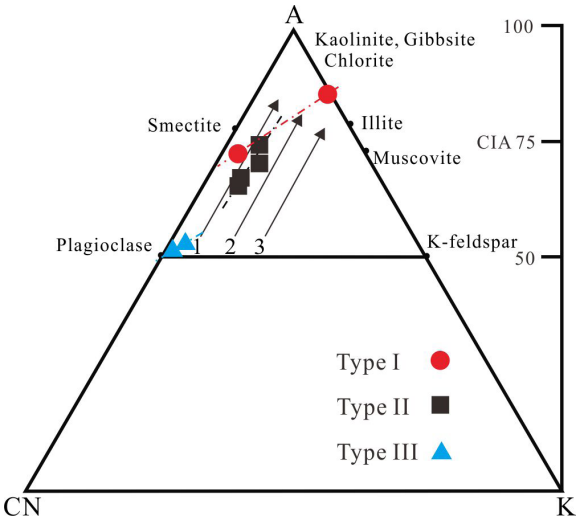

Text-fig. 9. A-CN-K diagram for the three types of the Zongzhuo Formation sandstones (after Nesbitt and Young 1982). Arrows 1–3 represent the weathering trends of andesite, granodiorite and granite, respectively.

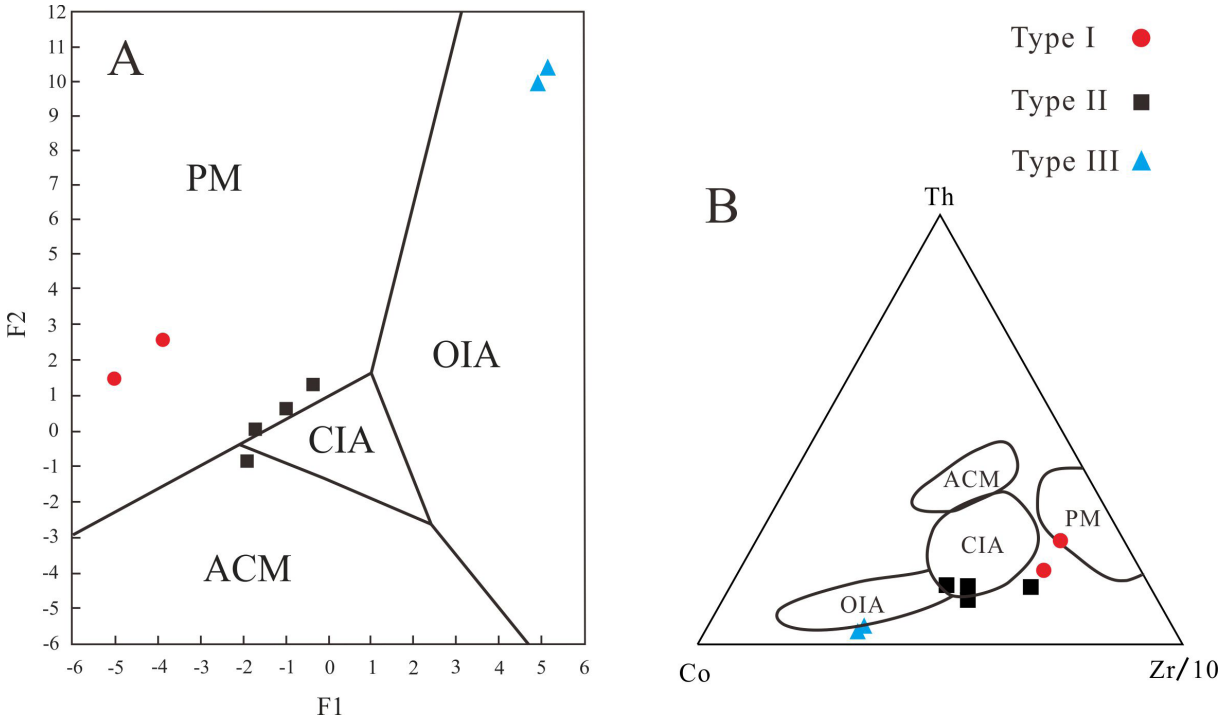

Text-fig. 10. Tectonic setting discrimination diagrams for the Zongzhuo Formation sandstones, A – following Bhatia (1983) and B – following Bhatia and Crook (1986). Explanations: PM – passive margin; ACM – active continental margin; CIA – continental island arc; OIA – oceanic island arc.

(52.49–54.09), indicating a cold, dry source area with low weathering. A marked drop in temperature and humidity can result from tectonic uplift, which is an increase in the altitude of the source area and the onset of the latest ice age (Fedo *et al.* 1995).

Tectonic setting

The geochemical compositions of sandstones from various tectonic environments in the source area can exhibit considerable divergence (Bhatia and Taylor 1981; Bhatia 1983, 1985; Bhatia and Crook 1986). We analyzed the average major and trace element contents in the three sandstone types to identify the tectonic setting of their source areas (Appendix 1). Type I and II sandstones were distinguished by SiO_2, low Al_2O_3, TFe_2O_3+MgO, CaO+Na_2O+K_2O, and Ti contents, with Type I sandstones aligned closely with passive margin (PM) characteristics. Type II sandstones demonstrated values consistent with both the passive margin and island arc settings. Type III sandstones contrasted sharply, presenting high Al_2O_3, TFe_2O_3+MgO, CaO+Na_2O+K_2O, Ti, and low SiO_2, similar to an island arc environment. Trace element characteristics also varied among the types (Appendix 2). The key parameters for Type I sandstones (e.g., Co, Cu, Ga, Hf, Pb, Sr, Zr, La, and Ce contents and LREE/HREE, La_N/Yb_N, K/Rb, Ba/Sr, K/Th, Th/U, Zr/Y, and Ti/Zr ratios) were closely aligned with those characteristic of a passive margin. In contrast, Type II sandstones shared characteristics with both PM and island arc settings, whereas the characteristics of Type III sandstones resembled those of island arcs and were distinct from those of continental margins.

Major and trace element data were calculated and plotted for the three sandstone types in the Zongzhuo Formation (Text-fig. 10). Using the F1–F2 function formula proposed by Bhatia (1983), we plotted the major element data in the F1–F2 discrimination diagram (Text-fig. 10A), where Type I and II sandstones primarily fell within the PM field, with Type II trending toward the CIA field. Type III sandstones were distinctly located in the OIA field and far from the other types. Similar patterns were observed in the Th–Co–Zr/10 diagram (Text-fig. 10B). Type I sandstones were plotted in the PM field, while Types II and III primarily fell near the CIA and OIA fields, respectively.

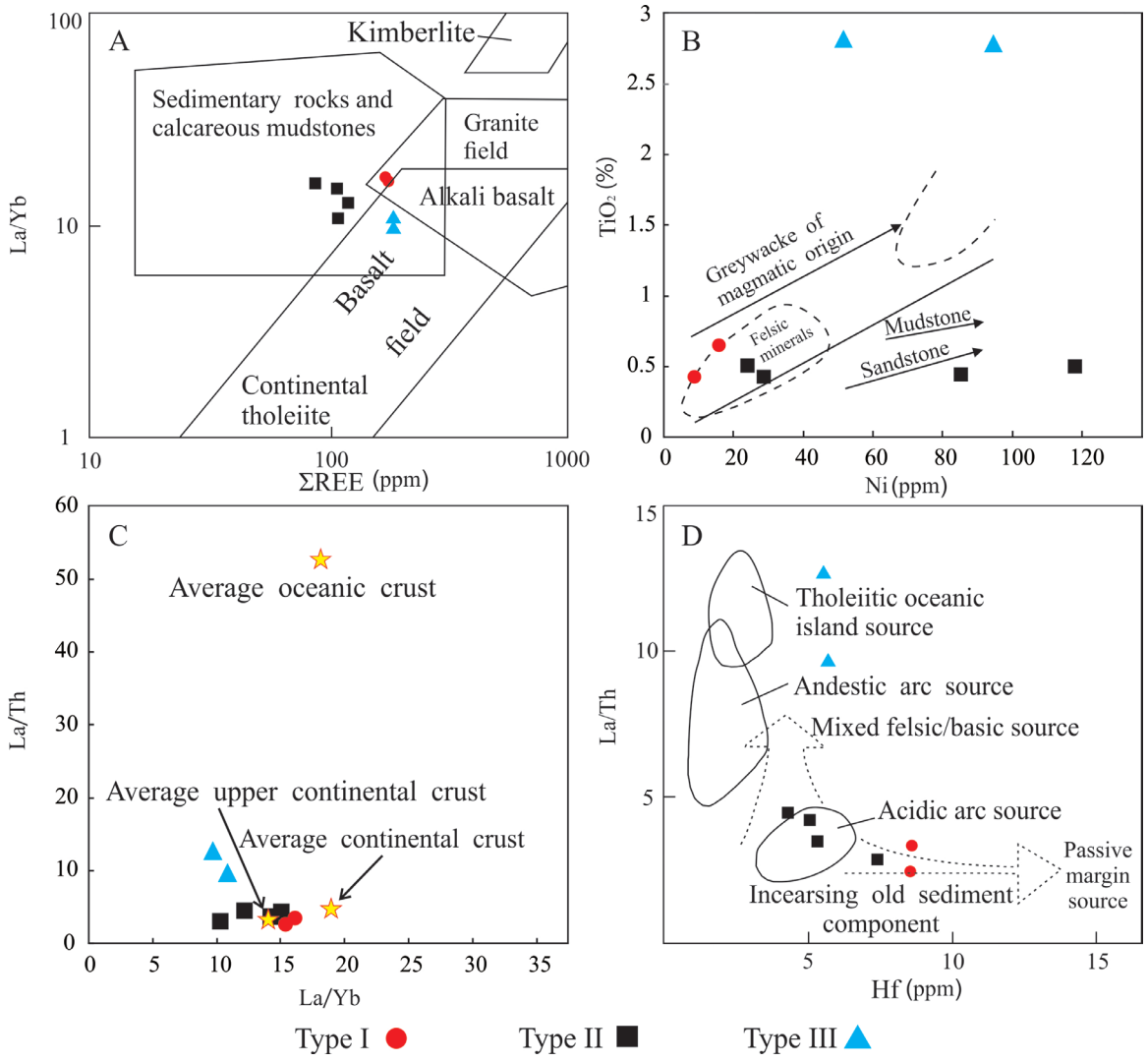

Text-fig. 11. Provenance discrimination diagrams for the three types of the Zongzhuo Formation sandstones. A – ΣREE vs. La/Yb (after Allègre and Minster 1978), B – Ni vs. TiO2 (after Floyd *et al*. 1989), C – La/Yb vs. La/Th (after Floyd and Leveridge 1987); D – Hf vs. La/Th (after Floyd and Leveridge 1987).

A comparison of the parameters and tectonic setting diagrams yielded consistent results. Type I sandstones from the early sedimentary stage of the Zongzhuo Formation exhibited geochemical characteristics typical of passive margin clastic deposition and were closely aligned with the passive margin sandstones. Type II sandstones deposited during the middle sedimentary stage shared passive margin geochemical features but with an increased influx of material from an island arc source. The latest Type III sandstones presented strong geochemical similarities with the OIA-derived sandstones, suggesting an OIA source area (Bhatia and Taylor 1981; Bhatia 1983, 1985; Bhatia and Crook 1986).

Provenance

Type I sandstones of the Zongzhuo Formation exhibited high levels of component and textural maturity, with detrital composition statistics indicating that quartz grains dominated the sandstone composition. Dickinson diagrams indicated recycled orogen provenance, and geochemical analysis revealed high SiO_2, low Al_2O_3, and low mafic mineral content. In the ΣREE–La/Yb diagram (Text-fig. 11A), the Type I samples fell within overlapping regions of sedimentary rocks and granites. In the Ni–TiO_2 and La/Yb–La/Th diagrams, Type I sandstones were plotted between the average continental upper crust

and average continental crust, suggesting a felsic source (Text-fig. 11A and 11B). In the Hf-La/Th diagram (Text-fig. 11D), they plotted between the acidic arc source field and passive margin source field. These indicators suggested that Type I sandstones represented typical passive margin deposits, with sedimentary materials likely sourced from nearby shield or platform sedimentary sequences (Bhatia 1983). Geochemical analysis indicated that the source of the Type I sandstones was likely felsic sedimentary rocks. In summary, Type I sandstones of the Zongzhuo Formation were probably derived from a single provenance, the Indian continent, which also supplied sedimentary material for other highly mature quartz sandstones in the Tethys Himalaya strata (Cai *et al.* 2011; An *et al.* 2017; Cheng J. *et al.* 2017; Xu K.Z. *et al.* 2019).

The detrital composition of the Type II sandstones resembles that of the Type I sandstones, with slightly lower maturity, less quartz, and more debris grains. Type II samples plotted near the center of the recycled orogen provenance field. Geochemically, Type II sandstones are characterized by slightly lower SiO_2, higher Al_2O_3, and increased mafic mineral content. Type II sandstones plotted near the sedimentary source, similar to the plot of average continental crust (Text-fig. 10A and 10C). In the Ni–TiO_2 and Hf–La/Th diagrams (Text-fig. 11B and 11D), these sandstones indicated a clear transition from a felsic to a mafic source and from ancient sediments to an acidic arc, suggesting a mixed acidic/basic source. These results indicated that Type II sandstones exhibited intermediate petrological and geochemical characteristics, transition trends, and mixed sources. Additionally, the tectonic setting for Type II sandstones demonstrated progression from a passive margin to an island arc. Therefore, Type II sandstones were likely derived from two sources: the Indian continent and the Lhasa Terrane.

With a high debris content, primarily volcanic, the Type III samples plotted within the island arc source and transition recycled fields (Text-fig. 5). These sandstones had notably low SiO_2, high Al_2O_3, elevated mafic mineral and TiO_2 contents, and REE patterns similar to those of the OIB, aligning with an oceanic island arc tectonic setting. In the ΣREE–La/Yb and Ni–TiO_2 diagrams (Text-fig. 11A and 11B), Type III sandstones indicated stronger basaltic and mafic sources than other sandstones. Furthermore, the Type III samples approached the tholeiitic oceanic island source field or trended toward the average oceanic crust field in the La/Yb–La/Th and Hf La/Th diagrams (Text-fig. 11C and 11D), supporting an island arc origin.

The relative age probabilities of Type III sandstones are illustrated in Text-fig. 12. The zircon ages were primarily concentrated around the main peak at 90 Ma, with a few ages near 500–1000 Ma. This detrital zircon age distribution closely resembled those of other Zongzhuo Formation sandstones from the Gyangze, Nagarze, and Bainang areas; Group 2 sandstones from the Xiukang Mélange; and sandstones from the Upper Ngamring, Padana, and Rilang Formations, as well as the Sangdanlin and Zheya sandstones, all of which can originate from the Lhasa Terrane (Cai *et al.* 2011; Wang J.G. *et al.* 2011; DeCelles *et al.* 2014; Wu *et al.* 2014; An *et al.* 2017; Cheng *et al.* 2017; Zhou *et al.* 2018). This age pattern is distinctly different from that of the Indian continent-derived Tethys Himalaya sandstones (e.g., Weimei Formation sandstones, Group 1 quartz sandstones of the Xiukang Mélange, and Jiabula Formation sandstones), which feature age peaks around 500–950 Ma and lack zircon ages younger than 500 Ma (Cai *et al.* 2011; Wu *et al.* 2014; Du *et al.* 2015; An *et al.* 2017; Xu K.Z. *et al.* 2019). In summary, Type III sandstones with their oceanic island arc-like tectonic setting, high volcanic debris content, geochemical resemblance to basic arc volcanic rocks, and similar detrital zircon age distribution to Lhasa Terrane-sourced strata indicated a provenance distinct from the other two types, which was likely sourced from the young volcanic rocks of the Lhasa Terrane.

Provenances feed model and tectonic evolution

The Late Cretaceous marked a pivotal geological period for the Tethys Himalayas. Following full subduction of the Neo-Tethys, the Tethys Himalaya transitioned from a passive margin to a foreland basin before colliding with the Asian continent, a continental collision that continued until the Oligocene (Mercier *et al.* 1987; Deng *et al.* 1995; Zhu *et al.* 2004). The Zongzhuo Formation deposited exclusively in the Tethys Himalaya during the Late Cretaceous preserves sedimentary deposits that may contain valuable information on source areas, helping clarify the relationships between provenance feed models and tectonic evolution.

This study identified three types of Zongzhuo Formation sandstones based on their petrology, geochemistry, and geochronology. Type I sandstones deposited during the early sedimentary stage of the Zongzhuo Formation exhibited high maturity, abundant felsic minerals, and low mafic mineral content, characteristic of terrigenous clastic deposits

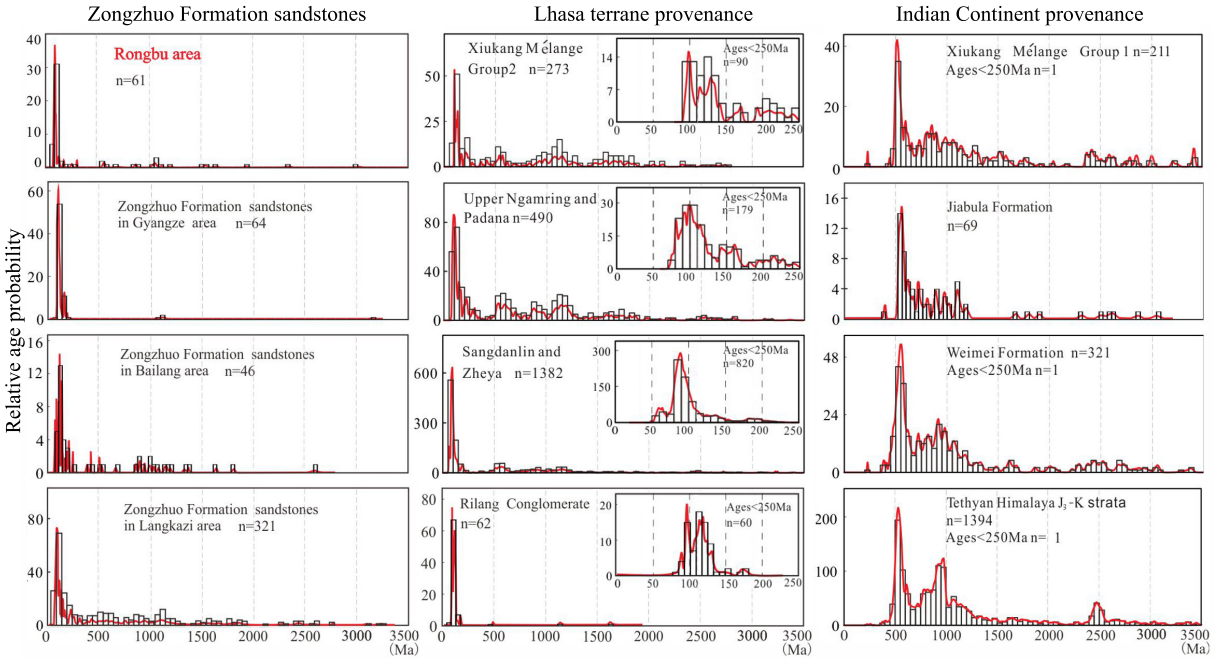

Text-fig. 12. Detrital zircon U-Pb age comparisons of the Zongzhuo Formation sandstones from different areas and the Tethys Himalaya strata sourced from different provenances. Data source: Zongzhuo Formation sandstones in the Rongbu area are from this study; Gyangze area is from Cai *et al.* (2011); Bailang area is from Cheng *et al.* (2017); Langkazi area is from Zhou *et al.* (2018); Xiukang Mélange Group 2 is from An *et al.* (2017); Upper Ngamring and Padana is from Wu *et al.* (2010) and An *et al.* (2014); Sangdanlin and Zheya are from Wang J.G. *et al.* (2011), DeCelles *et al.* (2014) and Wu *et al.* (2014); Rilang Conglomerate is from Cai *et al.* (2011); Xiukang Mélange Group 1 is from An *et al.* (2017); Weimei Formation is from Cai *et al.* (2011), Wu *et al.* (2014), Du *et al.* (2015) and An *et al.* (2017); Jiabula Formation is from Cai *et al.* (2011); Tethyan Himalaya J_3–K strata are from Hu *et al.* (2010), Cai *et al.* (2011), Gehrels *et al.* (2011), Zhu *et al.* (2011), Wu *et al.* (2014) and Du *et al.* (2015)

in a passive margin, derived from ancient sedimentary rocks of the Indian continent. Current research suggests that the Neo-Tethys ceased expanding and began subducting beneath the Lhasa Terrane in the Early Cretaceous, with subduction continuing into the early Late Cretaceous. Type I sandstone deposits were aligned with this perspective. The Neo-Tethys was not entirely subducted, and Type I sandstones were deposited along the Tethys Himalaya passive margin, resembling the earlier Weimei Formation and Jiabula sandstones sourced from the Indian continent (Text-fig. 13).

Second, Type II sandstones deposited during the middle sedimentary stage of the Zongzhuo Formation exhibit slightly lower maturity, reduced felsic mineral content, increased debris, and higher mafic mineral content. Their tectonic setting was dual, exhibiting characteristics of both passive margin and island-arc deposition. Provenance analysis indicated that the sedimentary materials for Type II sandstones were sourced simultaneously from the Indian continent and the Lhasa Terrane. The emergence of Type II sandstones suggests that the Neo-Tethys oceanic crust was fully subducted beneath the Lhasa Terrane, bringing the Tethys Himalaya into direct contact with the Lhasa Terrane and enabling bidirectional provenance input (Text-fig. 13).

Finally, the Type III lithic sandstones or graywackes deposited during the late sedimentary stage of the Zongzhuo Formation demonstrate low maturity, high mafic mineral content, abundant volcanic debris, short-distance deposition, and REE patterns similar to those of OIB. The tectonic setting of the source area resembled that of a continental island arc. The lithogeochemical characteristics and detrital zircon age models indicate that the Type III sandstones were sourced from young basic volcanic rocks of the Lhasa Terrane. As the India–Asia continental collision commenced during this stage, the Tethys Himalaya transitioned from a passive margin to a foreland basin at a convergent boundary, with sediment primarily sourced from the Lhasa

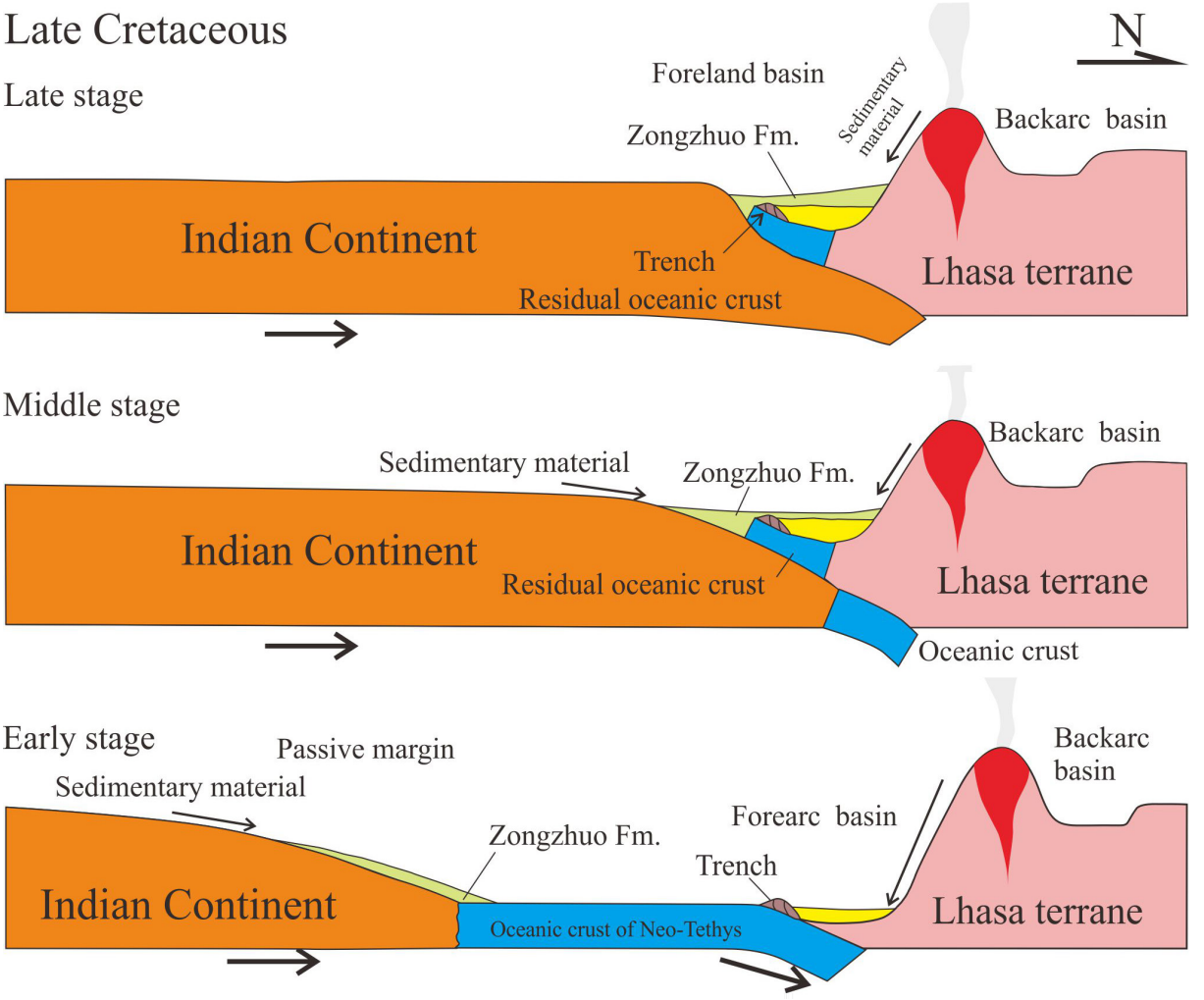

Text-fig. 13. Tectonic evolution of the Tethys Himalaya in the Late Cretaceous, including the source supply mode for the Zongzhuo Formation sandstones.

Terrane (Text-fig. 13). This intense collision introduced exotic blocks into the sedimentary process of the Zongzhuo Formation, which contributed to the formation of the mélange.

CONCLUSIONS

– Type I sandstones of the Zongzhuo Formation exhibit high maturity, with the clastic components primarily consisting of quartz grains. They are characterized by high felsic, low mafic, and low clay mineral contents, indicative of long-distance transport and REE patterns similar to those of the Weimei Formation sandstones and passive margin sedimentary rocks. In Type II sandstones, quartz grains prevail, while the felsic content and maturity are lower than those in Type I. There is a relative increase in both felsic and clay minerals, and the REE patterns are aligned using the passive margin model. Type III sandstones demonstrate the lowest maturity, indicating a nearby source with abundant debris particles, high mafic content, elevated clay minerals, TiO_2, and REE patterns resembling those of basic OIB magmatic rocks.

– Type I sandstones represent a typical terrigenous clastic rock deposited in a passive margin. They exhibit high weathering levels and were sourced from the Indian continent, being deposited in the Tethys Himalaya passive margin. Type II sandstones display moderate weathering from the source and dual characteristics of tectonic setting and provenance, suggesting simultaneous sourcing from the Indian

continent and the Lhasa Terrane. Type III sandstones exhibit low weathering grades, similar to the sandstones from an oceanic island arc, with geochemical data and U-Pb zircon dating indicating that the sedimentary material was likely derived from young basic volcanic rocks of the Lhasa Terrane.

– Type I sandstones deposited during the early sedimentary stage of the Zongzhuo Formation represented the Late Cretaceous deposits in the Tethys Himalaya, when the Neo-Tethys was not fully subducted and lacked contributions from the Lhasa Terrane material. Type II sandstones formed in the middle sedimentary stage were deposited in a passive margin setting, receiving sediment from both the Indian continent and the Lhasa Terrane, marking the last phase of the Tethys Himalaya as a passive margin. The latest Type III sandstones, primarily sourced from the Lhasa Terrane, signified the Tethys Himalaya transition to a foreland basin at the onset of the India–Asia continental collision.

Acknowledgements

The 1:50,000 regional geological survey projects in the Rongbu area were primarily conducted by the Chengdu University of Technology. This Level 2 project, part of the Gangdese–Himalayan Copper Resource Base Survey (project code: DD20160015–06), was supported by central funding. I extend my sincere gratitude to the Rongbu project team for their assistance in the field and their valuable comments and suggestions. We greatly thank two anonymous reviewers and Anna Żylińska (Editor) for their valuable comments and remarks that improved the quality of the manuscript.

REFERENCES

Ali, J.R. and Aitchison, J.C. 2008. Gondwana to Asia: Plate tectonics, paleogeography and the biological connectivity of the Indian sub-continent from the Middle Jurassic through latest Eocene (166–35 Ma). *Earth-Science Reviews*, **88** (3–4), 145–166.

Allègre, C.J. and Minster, J.F. 1978. Quantitative models of trace element behavior in magmatic processes. *Earth and Planetary Science Letters*, **38** (1), 1–25.

An, W., Hu, X.M. and Garzanti, E. 2017. Sandstone provenance and tectonic evolution of the Xiukang Mélange from Neotethyan subduction to India–Asia collision (Yarlung-Zangbo suture, south Tibet). *Gondwana Research*, **41**, 222–234.

An, W., Hu, X., Garzanti, E., BouDagher-Fadel, M.K., Wang, J. and Sun, G. 2014. Xigaze forearc basin revisited (South Tibet): provenance changes and origin of the Xigaze ophiolite. *Geological Society of America Bulletin*, **126**, 1595–1613.

Bhatia, M.R. 1983. Plate tectonics and geochemical composition of sandstones. *The Journal of Geology*, **91** (6): 611–627.

Bhatia, M.R. 1985. Rare earth element geochemistry of Australia paleozoic graywackes and mudrocks: provenance and tectonic control. *Sedimentary Geology*, **45**, 97–113.

Bhatia, M.R. and Crook, K.A.W. 1986. Trace element characteristics of graywackes and tectonic setting discrimination of sedimentary basins. *Contributions to Mineralogy and Petrology*, **92**, 181–193.

Bhatia, M.R. and Taylor, S.R. 1981. Trace-element geochemistry and sedimentary provinces: A study from the Tasman Geosyncline, Australia. *Chemical Geology*, **33**(1), 115–125.

Cai, F.L., Ding, L. and Yue, Y.H. 2011. Provenance analysis of upper Cretaceous strata in the Tethys Himalaya, southern Tibet: Implications for timing of India–Asia collision. *Earth and Planetary Science Letters*, **305**(1), 195–206.

Chen, L., Liu, Y., Hu, Z., Gao, S., Zong, K. and Chen, H. 2011. Accurate determinations of fifty-four major and trace elements in carbonate by LA-ICP-MS using normalization strategy of bulk components as 100%. *Chemical Geology*, **284**, 283–295.

Chen, X., Wang, C.S., Hu, X.M., Huang, Y.J., Wei, Y.S. and Wang, P.K. 2016. Petrology and evolution history from Late Jurassic to Paleogene of Gyangze basin, Southern Tibet. *Acta Petrologica Sinica*, **24** (3), 616–624.

Cheng, J., Shi, W. G., Zhang, W.F., Guo, J., Zhai, J. and Mi, M.W.J. 2017. Ages and provenance of the Zongzhuo Formation of melanges in Bailang area, Southern Xizang (Tibet): Evidence from Petrology and Detrital Zircon U–Pb Geochronology. *Geological Review*, **63** (06), 1440–1450.

Cullers, R.L. 2000. The geochemistry of shales, siltstones and sandstones of Pennsylvanian–Permian age, Colorado, USA: implications for provenance and metamorphic studies. *Lithos*, **51** (3), 181–203.

Cullers, R.L. 2002. Implications of elemental concentrations for provenance, redox conditions, and metamorphic studies of shales and limestones near Pueblo, CO, USA. *Chemical Geology*, **191** (4), 305–327.

DeCelles, P.G., Gehrels, G.E., Najman, Y., Martin, A.J., Carter, A. and Garzanti, E. 2004. Detrital geochronology and geochemistry of Cretaceous–Early Miocene strata of Nepal: implications for timing and diachroneity of initial Himalayan orogenesis. *Earth and Planetary Science Letters*, **227** (3–4), 313–330.

DeCelles, P.G., Gehrels, G.E., Quade, J., LaReau, B. and Spurlin, M. 2000. Tectonic implications of U-Pb zircon ages of the Himalayan Orogenic Belt in Nepal. *Science*, **288** (5465), 497–499.

DeCelles, P.G., Kapp, P., Gehrels, G.E. and Ding, L. 2014. Paleocene–Eocene foreland basin evolution in the Himalaya

of southern Tibet and Nepal: implications for the age of initial India–Asia collision. *Tectonics*, **33**, 824–849.

Deng, J.F., Zhao, H.L. and Lai, S.C. 1995. Intracontinental Orogenic Igneous Rocks and Orogenic Processes in Qinghai-Xizang Himalaya. *Journal of Earth Science*, **6** (2), 5–12.

Dickinson, W.R. 1970. Interpreting detrital modes of graywacke and arkose. *Journal of Sedimentary Petrology*, **40**, 695–707.

Dickinson, W.R. 1985. Interpreting provenance relations from detrital modes of sandstone. In: Zuffa, G.G. (Ed.), Provenance of Arenites, 333–361. Reidel; Dordrecht.

Dickinson, W.R., Bread, L.S., Brakenridge, G.R., Erjavec, J.L., Ferguson, R.C., Inman, K.F., Knepp, R.A., Lindberg, F.A. and Ryberg, P.T. 1983. Provenance of North American Phanerozoic sandstones in relation to tectonic setting. *Geological Society of America Bulletin*, **94**, 222–235.

Dickinson, W.R. and Suczek, C.A. 1979. Plate tectonics and sandstone compositions. *AAPG Bulletin*, **63** (12), 2164–2184.

Du, X.J., Chen, X., Wang, C.S., Wei, Y.S., Li, Y.L. and Jansa, L. 2015. Geochemistry and detrital zircon U–Pb dating of Lower Cretaceous volcaniclastics in the Babazhadong section, Northern Tethyan Himalaya: implications for the breakup of Eastern Gondwana. *Cretaceous Research*, **52**, 127–137.

Fedo, C.M., Nesbitt, H.W. and Young, G.M. 1995. Unraveling the effects of potassium metasomatism in sedimentary rocks and paleosols, with implications for paleoweathering conditions and provenance. *Geology*, **23**(10), 921–924.

Feng, L.J., Chu, X.L., Zhang, Q.R. and Zhang, T.G. 2003. CIA (Chemical index of alteration) and its applications in the Neoproterozoic clastic rocks. *Earth Science Frontiers*, **10** (04), 539–544.

Floyd, P.A. and Leveridge, B.E. 1987. Tectonic environment of the Devonian Gramscatho basin, south Cornwall: Framework mode and geochemical evidence from turbidite sandstones. *Journal of the Geological Society*, **144**(4), 531–542.

Floyd, P.A., Winchester, J.A. and Park, R.G. 1989. Geochemistry and tectonic setting of Lewisian clastic metasediments from the Early Proterozoic Loch Maree Group of Gairloch, NW Scotland. *Precambrian Research*, **45**(1), 203–214.

Fu, H.P., Hu, X.M., Crouch, E.M., An, W., Wang, J.G. and Garzanti, E. 2018. Upper Cretaceous trench deposits of the Neo-Tethyan subduction zone: Jiachala Formation from Yarlung Zangbo suture zone in Tibet, China. *Science China Earth Sciences*, **61**, 1204–1220.

Gao, L.F. 2006. Jurassic–Cretaceous boundary strata in southern Tibet, 107 pp. China University of Geosciences; Beijing.

Gazzi, P. 1966. Le arenarie del flysch sopracretaceo dell' Appennino modenese: Correlazione con il flysch di Monghidoro. *Mineralogica et Petrographica Acta*, **12**, 69–97.

Gehrels, G., Kapp, P., DeCelles, P., Pullen, A., Blakey, R., Weislogel, A., Ding, L., Guynn, J., Martin, A., McQuarrie, N. and Yin, A. 2011. Detrital zircon geochronology of pre-Tertiary strata in the Tibetan–Himalayan orogen. *Tectonics*, **30** (5), TC5016.

Hanchar, J.M. and Miller, C.F. 1993. Zircon zonation patterns as revealed by cathodoluminescence and backscattered electron images: Implications for interpretation of complex crustal histories. *Chemical Geology*, **110** (1), 1–13.

Hoskin, P.W.O. and Black, L.P. 2000. Metamorphic zircon formation by solid-state recrystallization of protolith igneous zircon. *Journal of Metamorphic Geology*, **18** (4), 423–439.

Hu, X.M., Garzanti, E., An, W. and Hu, X.F. 2015. Provenance and drainage system of the Early Cretaceous volcanic detritus in the Himalaya as constrained by detrital zircon geochronology. *Journal of Palaeogeography*, **4** (1), 85–98.

Hu, X.M., Jansa, L, Chen, L., Griffin, W.L., O'Reilly, S.Y. and Wang, J.G. 2010. Provenance of Lower Cretaceous Wölong volcaniclastics in the Tibetan Tethyan Himalaya: Implications for the final breakup of Eastern Gondwana. *Sedimentary Geology*, **223** (3–4), 193–205.

Huang, X.D. 2011. Study on metallogenic regularity and ore-prospecting direction of Gyantse-Lhunze gold-antimony metallogenic belt in the South Tibetan Detachment System. Unpublished thesis, Chengdu University of Technology; Chengdu. [In Chinese]

Huang, Y., Liang, W., Zhang, L.K., Li, G.M., Huang, C.M., Xia, X.B., Dong, S.L. and Wu, J.Y. 2018. The initial breakup between Tethyan–Himalaya and Indian Terrane: Evidences from Late Cretaceous OIB-type basalt in Southern Tibet. *Earth Science*, **43** (08), 2651–2663.

Liu, Y.S., Gao, S., Hu, Z.C., Gao, C.G., Zong, K.Q. and Wang, D.B. 2010. Continental and oceanic crust recycling-induced melt-peridotite interactions in the Trans-North China Orogen: U-Pb dating, Hf isotopes and trace elements in zircons of mantle xenoliths. *Journal of Petrology*, **51** (1–2), 537–571.

Liu, Y.S., Hu, Z.C., Gao, S., Gunther, D., Xu, J., Gao, C. and Chen, H. 2008. In situ analysis of major and trace elements of anhydrous minerals by LA-ICP-MS without applying an internal standard. *Chemical Geology*, **257**(1), 34–43.

Ludwig, K.R. 2003. Isoplot 3.00: A geochronological toolkit for Microsoft Excel, 50 pp. Berkeley Geochronology Center; Berkeley.

McLennan, S.M., Hemming, S.R., McDaniel, D.K. and Hanson, G.N. 1993. Geochemical approaches to sedimentation, provenance, and tectonics. In: Johnsson, M.J. and Basu, A. (Eds), Processes controlling the composition of clastic sediments. *Geological Society of America, Special Paper*, **284**, 21–40.

Mercier, J.L., Armijo, R., Tapponnier, P., Carey-Gailhardis, E. and Lin, H.T. 1987. Change from Late Tertiary compression to Quaternary extension in southern Tibet during the India–Asia Collision. *Tectonics*, **6** (3), 275–304.

Möller, A., O'Brien, P.J., Kennedy, A. and Körner, A. 2003. Linking growth episodes of zircon and metamorphic

textures to zircon chemistry: an example from the ultra-high-temperature granulites of Rogaland (SW Norway). *Geological Society of London Special Publications*, **220** (1), 65–81.

Nesbitt, H.W. and Young, G.M. 1982. Early Proterozoic climates and plate motions inferred from major element chemistry of lutites. *Nature*, **299**, 715–717.

Nesbitt, H.W. and Young, G.M. 1989. Formation and diagenesis of weathering profiles. *Journal of Geology*, **97**, 129–147.

Nie, F.J., Hu, P., Jiang, S.H., Li, Z.Q., Liu, Y. and Zhou, Y.Z. 2005. Type and temporal-spatial distribution of gold and antimony deposits (prospects) in Southern Tibet, China. *Acta Geologica Sinica*, **79** (3), 373–385.

Pan, G.T., Chen, Z.L., Li, X.Z., Yan, Y.J., Xu, X.S., Xu, Q., Jiang, X.S., Wu, Y.L., Luo, J.N., Zhu, T.X. and Peng, Y.M. 1997. Formation and evolution of the Eastern Tethyan geological structure, 218 pp. Geological Publishing House; Beijing.

Song, B., Zhang, Y.H., Wan, Y.S. and Jian, P. 2002. Mount making and procedure of the SHRIMP Dating. *Geological Review*, **48** (S1), 26–30. [In Chinese]

Sun, G.Y., Hu, X.M. and Wang, J.G. 2011. Petrologic and provenance analysis of the Zongzhuo Mélange in Baisha Area, Gyangze, Southern Tibet. *Acta Geologica Sinica*, **85** (08), 1343–1351.

Sun, S.S. and McDonough, W.F. 1989. Chemical and isotopic systematics of oceanic basalts: Implications for mantle composition and processes. In: Saunders, A.D. and Norry, M.J. (Eds), Magmatism in the Ocean Basins. *Special Publications of the Geological Society of London*, **42**, 313–345.

Wang, C.S., Li, X.H., Wan, X.Q. and Tao, R. 2000. The Cretaceous in Gyangze, Southern Xizang (Tibet): redefined. *Acta Geologica Sinica*, **74** (02), 97–105.

Wang, J.G., Hu, X.M., Jansa, L. and Huang, Z.C. 2011. Provenance of the Upper Cretaceous–Eocene deep-water sandstones in Sangdanlin, Southern Tibet: constraints on the timing of initial India–Asia collision. *The Journal of Geology*, **119**, 293–309.

Wiedenbeck, M., Allé, P., Corfu, F., Griffin, W.L., Meier, M., Oberli, F., Quadt, A.V., Roddick, J.C. and Spiegel, W. 1995. Three natural zircon standards for U-Th-Pb, Lu-Hf, trace element and REE analyses. *Geostandards Newsletter*, **19** (1), 1–23.

Wu, F.Y., Ji, W.Q., Liu, C.Z. and Chung, S.L. 2010. Detrital zircon U-Pb and Hf isotopic data from the Xigaze fore-arc basin: constraints on Transhimalayan magmatic evolution in southern Tibet. *Chemical Geology*, **271**, 13–25.

Wu, F.Y., Ji, W.Q., Wang, J.G., Liu, C.Z., Chung, S.L. and Clift, P.D. 2014. Zircon U–Pb and Hf isotopic constraints on the onset time of India–Asia collision. *American Journal of Science*, **314**, 548–579.

Xia, D.X. and Liu, S.K. 1997. Lithostratigraphy of Tibet Autonomous Region, 302 pp. China University of Geosciences Press; Wuhan.

Xu, K.Z., Ding, F., Li, Q., X, X.G., Yang, L., Li, Y. and Dong, B.B. 2019. Petrology and geochemistry of Upper Jurassic Weimei Formation sandstones in southern Tibet: implications for provenance and tectonic setting. *Geosciences Journal*, **23**, 767–790.

Xu, Z.Q., Yang, J.S., Li, H.B., Ji, S.C., Zhang, Z.M. and Liu, Y. 2011. On the tectonics of the India–Asia Collision. *Acta Geologica Sinica*, **85** (1), 1–5.

Yang, T.S., Ma, Y.M., Bian, W.W., Jin, J.J., Zhang, S.H., Wu, H.C., Li, H.Y., Yang, Z.Y. and Ding, J.K. 2015. Paleomagnetic results from the Early Cretaceous Lakang Formation lavas: Constraints on the paleolatitude of the Tethyan Himalaya and the India–Asia Collision. *Earth and Planetary Science Letters*, **428**, 120–133.

Yi, Z.Y., Liang, Y.L., Zhao, J., Yan, Y.G., Chen, L.W. and Tang, X.D. 2016. Paleogeography of the Northern Margin of Indian Continent Prior to Its Collision An investigation of the Late Cretaceous limestones in south Tibet. *Acta Geologica Sinica*, **90** (11), 3282–3292.

Zhang, B.X., Li, Y.X. and Hu, X.M. 2017. Paleomagnetic results from Jurassic–Cretaceous strata in the Chuangde area of southern Tibet constrain the nature and timing of the India–Asia collision system. *Chinese Science Bulletin*, **62** (04), 298–314. [In Chinese]

Zhou, B., Hu, X.M., An, W., Ma, A.L. and Lai, W. 2018. Trench deposition during the initial Indian–Asian collision: petrologic and provenance analysis of the Zongzhuo Formation, southeastern Tibet. *Acta Geologica Sinica*, **92** (01), 1–14.

Zhu, D.C., Mo, X.X., Zhao, Z.D., Niu, Y.L., Pan, G.T., Wang L.Q. and Liao, Z.L. 2009. Permian and Early Cretaceous tectonomagmatism in southern Tibet and Tethyan evolution: new perspective. *Earth Science Frontiers*, **16** (2), 1–20.

Zhu, D.C., Pan, G.T., Mo, X.X., Duan, L.P. and Liao, Z.L. 2004. The age of collision between India and Eurasia. *Advances in Earth Science*, **19** (04), 564–571.

Zhu, D.C., Xia, Y., Qiu, B.B., Wang, Q. and Zhao, Z.D. 2013. Why do we need to propose the Early Cretaceous Comei large igneous province in southeastern Tibet? *Acta Petrologica Sinica*, **29** (11), 3659–3670.

Zhu, D.C., Zhao, Z.D., Niu, Y.L., Dilek, Y. and Mo, X.X. 2011. Lhasa Terrane in southern Tibet came from Australia. *Geology*, **39** (8), 727–730.

Manuscript submitted: 15th April 2025
Revised version accepted: 16th January 2026

Appendix 1

U–Pb age data of detrital zircons from Zongzhuo Formation sandstones.

Spot	Content (ppm)		Th/U	U–Pb Isotope Ratio								U–Pb Isotopic Age (Ma)								Concordance
	Th	U		$^{207}Pb/^{206}Pb$		$^{207}Pb/^{235}U$		$^{206}Pb/^{238}U$		$^{208}Pb/^{232}Th$		$^{207}Pb/^{206}Pb$		$^{207}Pb/^{235}U$		$^{206}Pb/^{238}U$		$^{208}Pb/^{232}Th$		
				ratio	1σ	ratio	1σ	ratio	1σ	ratio	1σ	ratio	1σ	ratio	1σ	ratio	1σ	ratio	1σ	
Zongzhuo Fm.										Sample B07										
B07–01	2300	2025	1.136	0.0467	0.0021	0.1006	0.0046	0.0156	0.0002	0.0053	0.0001	35	107	97	4	100	1	107	3	97%
B07–02	188	425	0.442	0.0771	0.0019	2.0252	0.0513	0.1899	0.0017	0.0598	0.0012	1124	50	1124	17	1121	9	1175	24	99%
B07–03	360	248	1.452	0.1020	0.0024	4.0979	0.0969	0.2909	0.0033	0.0841	0.0016	1661	44	1654	19	1646	16	1633	31	99%
B07–04	321	150	2.138	0.0665	0.0030	1.3228	0.0559	0.1459	0.0020	0.0441	0.0010	833	97	856	24	878	12	873	19	97%
B07–05	427	522	0.817	0.0688	0.0018	1.3700	0.0359	0.1442	0.0017	0.0479	0.0009	894	54	876	15	868	9	946	17	99%
B07–07	404	408	0.990	0.0419	0.0055	0.1332	0.0068	0.0200	0.0025	0.0052	0.0002	error		127	6	128	16	105	5	99%
B07–08	91	166	0.546	0.0380	0.0048	0.2012	0.0184	0.0270	0.0006	0.0066	0.0005	error	error	186	16	172	4	133	10	91%
B07–09	261	411	0.635	0.0386	0.0047	0.0948	0.0083	0.0143	0.0004	0.0041	0.0003	error	error	92	8	91	2	82	5	99%
B07–10	774	597	1.296	0.0419	0.0030	0.0876	0.0052	0.0134	0.0002	0.0042	0.0001	error	error	85	5	86	1	86	3	99%
B07–11	494	628	0.787	0.0464	0.0044	0.0932	0.0085	0.0134	0.0002	0.0034	0.0002	20	215	90	8	86	2	69	3	94%
B07–12	429	519	0.826	0.0405	0.0037	0.1004	0.0071	0.0152	0.0003	0.0044	0.0002	error	error	97	7	97	2	89	4	99%
B07–13	450	500	0.900	0.0438	0.0033	0.1086	0.0060	0.0152	0.0003	0.0050	0.0002	error		105	5	97	2	101	4	92%
B07–14	873	928	0.941	0.0479	0.0028	0.0950	0.0050	0.0143	0.0002	0.0043	0.0001	100	133	92	5	91	2	88	3	99%
B07–15	1036	725	1.429	0.0473	0.0031	0.1006	0.0057	0.0148	0.0002	0.0047	0.0001	65	144	97	5	95	1	94	3	97%
B07–16	482	514	0.937	0.0513	0.0032	0.1500	0.0084	0.0208	0.0004	0.0066	0.0002	254	144	142	7	133	2	133	4	93%
B07–17	717	846	0.847	0.0476	0.0030	0.0951	0.0051	0.0137	0.0002	0.0041	0.0001	76	141	92	5	88	1	84	3	94%
B07–18	211	423	0.499	0.0444	0.0030	0.2567	0.0154	0.0399	0.0007	0.0124	0.0004	error		232	12	252	5	250	8	91%
B07–19	277	327	0.846	0.0385	0.0042	0.1148	0.0105	0.0182	0.0004	0.0048	0.0003	error	error	110	10	116	3	97	5	94%
B07–20	136	361	0.377	0.0439	0.0066	0.1030	0.0138	0.0141	0.0003	0.0027	0.0007	error		100	13	90	2	54	14	90%
B07–21	639	548	1.167	0.0409	0.0035	0.0981	0.0063	0.0156	0.0003	0.0048	0.0002	error	error	95	6	99	2	96	3	95%
B07–22	119	217	0.547	0.0306	0.0049	0.0962	0.0101	0.0139	0.0005	0.0028	0.0003	error	error	93	9	89	3	57	6	95%
B07–23	238	388	0.614	0.0377	0.0042	0.0974	0.0085	0.0157	0.0003	0.0033	0.0003	error	error	94	8	100	2	66	6	93%
B07–24	3280	2519	1.302	0.0481	0.0019	0.0907	0.0035	0.0137	0.0002	0.0043	0.0001	106	93	88	3	88	1	87	2	99%
B07–25	356	785	0.453	0.0462	0.0034	0.0950	0.0061	0.0139	0.0002	0.0044	0.0002	6	167	92	6	89	2	89	4	96%
B07–27	221	862	0.256	0.0746	0.0016	1.8414	0.0419	0.1786	0.0018	0.0540	0.0012	1057	43	1060	15	1059	10	1063	23	99%
B07–29	864	946	0.914	0.0445	0.0028	0.0814	0.0049	0.0133	0.0002	0.0040	0.0001	error		79	5	85	1	80	2	93%
B07–30	248	866	0.286	0.1189	0.0018	5.7722	0.0954	0.3511	0.0030	0.0994	0.0016	1940	28	1942	14	1940	15	1915	30	99%
B07–31	629	649	0.969	0.0484	0.0036	0.1082	0.0065	0.0151	0.0002	0.0049	0.0002	120	167	104	6	97	2	99	3	92%
B07–32	222	393	0.566	0.0373	0.0036	0.0946	0.0074	0.0147	0.0003	0.0043	0.0002	error	error	92	7	94	2	86	5	97%
B07–33	551	877	0.629	0.0499	0.0029	0.1002	0.0052	0.0141	0.0002	0.0047	0.0002	191	132	97	5	90	1	94	3	92%

B07–34	396	584	0.678	0.0414	0.0045	0.0898	0.0087	0.0142	0.0003	0.0041	0.0003	error	error	87	8	91	2	82	6	95%
B07–35	334	182	1.835	0.0857	0.0029	2.4459	0.0902	0.2057	0.0024	0.0651	0.0013	1331	65	1256	27	1206	13	1274	26	95%
B07–36	269	409	0.657	0.0629	0.0021	0.7815	0.0256	0.0898	0.0011	0.0289	0.0007	706	69	586	15	554	6	576	13	94%
B07–37	846	708	1.195	0.0449	0.0035	0.1022	0.0059	0.0143	0.0003	0.0048	0.0002	error		99	5	91	2	97	3	92%
B07–38	384	734	0.522	0.2470	0.0038	20.4301	0.3343	0.5966	0.0055	0.1602	0.0027	3166	24	3112	16	3016	22	3003	47	96%
B07–39	146	380	0.385	0.0495	0.0036	0.2092	0.0128	0.0280	0.0005	0.0093	0.0005	172	159	193	11	178	3	187	9	92%
B07–40	233	179	1.298	0.1016	0.0027	3.7546	0.1023	0.2679	0.0030	0.0777	0.0016	1654	50	1583	22	1530	15	1513	31	96%
B07–42	371	397	0.935	0.0764	0.0020	1.8742	0.0491	0.1773	0.0018	0.0524	0.0010	1106	56	1072	17	1052	10	1033	19	98%
B07–43	482	636	0.757	0.0456	0.0035	0.1140	0.0076	0.0159	0.0003	0.0048	0.0002	error		110	7	102	2	96	4	92%
B07–44	566	721	0.785	0.1566	0.0024	9.5386	0.1661	0.4392	0.0041	0.1182	0.0019	2420	31	2391	16	2347	18	2258	35	98%
B07–45	546	944	0.579	0.0733	0.0015	1.7611	0.0377	0.1735	0.0017	0.0509	0.0009	1022	40	1031	14	1031	9	1003	18	99%
B07–46	644	690	0.933	0.0487	0.0037	0.1037	0.0068	0.0146	0.0002	0.0045	0.0002	132	170	100	6	94	2	91	3	93%
B07–47	712	1740	0.410	0.0459	0.0021	0.0999	0.0044	0.0157	0.0002	0.0050	0.0002	error		97	4	100	1	101	3	96%
B07–50	565	765	0.739	0.0438	0.0032	0.0959	0.0056	0.0140	0.0002	0.0044	0.0002	error		93	5	90	2	89	4	96%
B07–53	235	899	0.262	0.0591	0.0017	0.7611	0.0218	0.0926	0.0010	0.0303	0.0008	572	61	575	13	571	6	604	16	99%
B07–54	1826	1325	1.378	0.0457	0.0024	0.0914	0.0042	0.0143	0.0002	0.0046	0.0001	error		89	4	92	1	92	2	96%
B07–55	997	1040	0.958	0.0496	0.0032	0.0968	0.0056	0.0136	0.0002	0.0046	0.0001	172	154	94	5	87	1	92	3	92%
B07–57	541	358	1.512	0.0761	0.0020	1.8907	0.0511	0.1795	0.0020	0.0536	0.0009	1098	47	1078	18	1064	11	1056	18	98%
B07–58	630	834	0.756	0.0572	0.0016	0.7236	0.0207	0.0919	0.0011	0.0284	0.0005	498	66	553	12	567	6	567	11	97%
B07–59	1643	1051	1.563	0.0498	0.0031	0.0967	0.0050	0.0135	0.0002	0.0044	0.0001	183	146	94	5	86	1	89	2	91%
B07–61	697	980	0.711	0.0466	0.0027	0.0917	0.0046	0.0140	0.0002	0.0046	0.0002	32	133	89	4	90	1	92	3	99%
B07–63	881	862	1.023	0.0491	0.0029	0.0982	0.0051	0.0135	0.0002	0.0043	0.0001	154	141	95	5	87	1	86	3	90%
B07–64	1025	936	1.095	0.0449	0.0031	0.0981	0.0057	0.0154	0.0003	0.0051	0.0001	error		95	5	98	2	103	3	96%
B07–65	873	998	0.875	0.0700	0.0017	1.1019	0.0541	0.1135	0.0050	0.0387	0.0017	928	51	754	26	693	29	767	33	91%
B07–67				0.0066	0.0045	0.3707	0.0052	0.0480	0.0003	0.0157	0.0002	error	error	320	4	302	2	316	5	94%
B07–68	531	674	0.789	0.0498	0.0033	0.0977	0.0059	0.0135	0.0002	0.0047	0.0002	187	156	95	5	86	2	95	3	90%
B07–69	447	323	1.386	0.0932	0.0020	3.4958	0.0744	0.2719	0.0026	0.0792	0.0013	1492	41	1526	17	1550	13	1541	24	98%
B07–70	1273	1774	0.718	0.0505	0.0023	0.0995	0.0045	0.0144	0.0002	0.0047	0.0001	217	106	96	4	92	1	95	2	95%
B07–71	1112	1079	1.031	0.0479	0.0023	0.1296	0.0059	0.0195	0.0003	0.0060	0.0001	95	117	124	5	125	2	120	3	99%
B07–73	367	480	0.764	0.0388	0.0039	0.1271	0.0072	0.0175	0.0010	0.0057	0.0005	error	error	121	7	112	6	116	9	91%
B07–74	937	1345	0.697	0.0499	0.0026	0.0987	0.0052	0.0142	0.0002	0.0045	0.0001	191	122	96	5	91	1	91	2	95%

Appendix 2

Comparison of the three types of Zongzhuo Formation sandstone and different source structures trace elements of sandstone. The major and trace element characteristics of the sandstones from the source areas in different tectonic environments are derived from Bhatia (1983) and Bhatia and Crook (1986).

Major elements (%)	Type I	Type II	Type III	OIA	CIA	ACM	PM
SiO_2	85.18	72.16	45.31	58.83±1.6	70.69±2.6	73.86±4.0	81.95±6.2
Al_2O_3	6.50	8.64	13.96	17.11±1.7	14.04±1.1	12.89±2.1	8.41±2.2
TFe_2O_3+MgO	3.19	6.70	16.96	11.73±3.53	6.79±1.44	4.29±2.00	4.67±3.73
CaO+Na_2O+K_2O	1.97	6.33	13.76	11.53±2.7	7.69±1.8	8.15±2.2	4.67±3.5
K	0.58	0.71	0.46	0.91±0.43	1.37±0.21	2.19±0.32	1.06±0.32
Ti	0.32	0.28	1.68	0.48±0.12	0.39±0.06	0.26±0.02	0.22±0.06
Trace elements (ppm)							
Co	8.71	13.85	43.44	18±6.3	12±2.7	10±1.7	5±2.4
Cu	7.41	16.90	43.96	23±13.1	11±3.3	8±3.1	6±2.6
Ga	10.36	9.86	19.16	17±1.9	13±1.3	14±1.5	8±1.6
Hf	8.57	5.53	5.60	2.1±0.6	6.3±2.0	6.800	10.100
Pb	16.89	12.72	2.45	6.9±1.4	15.1±1.1	24.0±1.1	16.0±3.4
Rb	28.12	41.65	8.37	18±10.7	67±10	115±8	61±19
Sr	48.97	120.12	267.54	637±516	250±86	141±30	66±22
Th	10.84	5.03	2.40	2.27±0.7	11.1±1.1	18.8±3.0	16.7±3.5
V	57.30	75.54	248.74	131±40	89±13.7	48±5.9	31±9.9
Zn	46.99	58.25	110.50	89±18.6	74±9.8	52±8.6	26±12
Zr	333.48	208.08	216.76	96±20	229±27	179±33	298±80
La	30.80	18.33	26.48	8.72±2.5	24.4±2.3	33.0±4.5	33.5±5.8
Ce	61.69	34.45	53.51	22.53±5.9	50.5±4.3	72.7±9.8	71.9±11.5
LREE/HREE	9.63	7.92	6.20	3.8±0.9	7.7±1.7	9.100	8.500
La_N/Yb_N	11.36	9.34	7.38	4.2±1.3	7.5±2.5	8.500	10.800
δEu	0.74	0.77	1.13	1.01±0.11	0.79±0.13	0.600	0.560
K/Rb	205.09	169.84	555.17	578±92	219±28	189±20	178±20
Rb/Sr	0.57	0.35	0.03	0.05±0.05	0.65±0.33	0.89±0.24	1.19±0.4
Ba/Sr	6.01	1.08	0.57	0.95±0.6	3.55±1.4	3.8±0.7	4.7±1.3
K/Th	532.01	1406.35	1936.17	4055±1526	1296±250	1252±360	681±194
K/U	3582.00	8522.81	6365.49	8682±4438	5631±867	5956±1560	3950±1382
Th/U	6.73	6.06	3.29	2.1±0.78	4.6±0.45	4.8±0.38	5.6±0.7
Zr/Th	30.76	41.37	90.32	48.0±13.4	21.5±2.4	9.5±0.7	19.1±5.8
Zr/Y	18.68	13.93	7.96	5.67±1.94	9.6±0.8	7.2±0.4	12.4±4.0
Ti/Zr	9.54	13.34	77.64	56.8±21.4	19.7±4.3	15.3±2.4	6.74±0.9